

THE SHORT-TERM PREDICTION OF UNIVERSAL TIME AND
LENGTH-OF-DAY USING ATMOSPHERIC ANGULAR MOMENTUM

by

A. P. Freedman

J. A. Steppe

J. O. Dickey

T. M. Eubanks*

L.-Y. Sung

Jet Propulsion Laboratory
California Institute of Technology
Pasadena, CA 91109

* now at U. S. Naval Observatory
Washington, DC 20390

Short Title: Predicting UT1 and LOD With AAM

February 1993

to be submitted to
Journal of Geophysical Research

1. Introduction

Development of high-precision space-age geodetic techniques during the last two decades has led to unprecedented accuracy in our knowledge of variations in the Earth's rate of rotation and orientation in space. These measurements have, in turn, led to greater understanding of the physical processes which influence Earth orientation, including atmospheric and oceanic motions, core-mantle interactions, and tidal forces. Earth orientation parameter values are regularly employed in, and are essential to, the fields of astronomy, astrometry, and celestial mechanics, among others. Of particular importance for the study presented here is the need for accurate Earth orientation to enable the precise tracking of interplanetary spacecraft. The Deep Space Network (DSN), operated by the Jet Propulsion Laboratory (JPL) for the National Aeronautics and Space Administration (NASA), requires continuous, real-time knowledge of Earth rotation and polar motion variations in order to precisely track and navigate interplanetary spacecraft such as **Magellan**, Galileo, Ulysses, and **Cassini** [Treuhaft and Wood, 1986; Runge, 1987; JPL, 1991].

Methods to combine the diverse set of geodetic measurements of Earth orientation that are currently available, and to interpolate and extrapolate these data to generate an optimal estimate of Earth orientation, have been under development at JPL for a number of years. The strategy currently in use is a **Kalman** filtering scheme based on Earth orientation parameters and their excitation functions that incorporates stochastic models of the important physical processes and takes into account the variable form, quality, and temporal density of the data provided by different measurement services [Morabito et al., 1988]. The Earth orientation series thus generated have been shown to be robust and of high quality, and to agree quite well with those generated by other institutions [King, 1990; IERS, 1992a; Grosset al., 1993].

Of the five components of Earth orientation—longitude ($d\psi$) and obliquity ($d\epsilon$) offsets of the celestial ephemeris pole, X and Y polar motion, and Universal Time (UT1)—the one which varies most dramatically and unpredictably from day to day, posing the greatest

challenge for real-time estimation, is UT1, Likening the rotating Earth to a timepiece, UT 1 is a measure of the angle about the polar axis through which the Earth has rotated, usually specified with respect to a reference time defined by atomic clocks (e.g., UT1–UTC or UT1 – TAI). UT1 is conventionally given in units of milliseconds of time, where 1 ms corresponds to an angle of approximately 73 nrad and an equatorial angular displacement of 46,5 cm.

Variations in the rate of change of UT1, dU/dt , are of great interest to the scientific and navigation communities, The excess length of the day A (often referred to as ΔLOD) is related to the UT1 rate-of-change (to first order in A/Λ_0) by

$$A = -\Lambda_0 \frac{dU}{dt} \quad (1)$$

where A is the difference between the true length of day and a nominal day of 86,400 seconds duration (Λ_0), and U represents UT1–TAI [Lambeck, 1980, for example], The quantity A will henceforth be referred to as LOD, even though it represents the excess length-of-day rather than the actual length of the day.

In order to correctly model the stochastic behavior of quantities such as UT1 and LOD, the effects of physical processes which influence the rotation rate in a known and predictable manner must be removed, Foremost among these are the solid-Earth and equilibrium ocean tides, which can be directly removed from UT1 and LOD by applying corrections obtained from conventional tidal models [Yoder et al., 1981]. Unless otherwise noted, UT1 (U) and LOD (A) refer here to these quantities with both long- and short-period tides removed (the UT1R' and LODR' of the IERS [1992a]). With tides removed, LOD typically varies by a few hundredths of a millisecond over a 24 hour period. On subseasonal time scales (i.e., less than a few months), LOD behaves as a random-walk stochastic process [Eubanks et al., 1985; Dickey et al., 1989; 1992].

The challenge of short-term UT1 prediction stems from the limitations implicit in a stochastic model for LOD: even if the model accurately characterizes the behavior of the time series in an average sense, particular episodes can be found when the LOD variability

substantially exceeds that typically expected. For example, LOD has appeared to vary monotonically by as much as 0.1 ms per day over several days. Given the present stochastic models for LOD and UT1 behavior, the errors in the predicted values of UT1 (i.e., those estimates of UT1 made after geodetic measurements are no longer available) during these episodes will exceed the accuracy level currently required by the DSN (about 0.6 ms) in less than 4 days. Although frequent geodetic measurements of UT1 are routinely being made, reducing the raw data and generating UT1 estimates ordinarily requires at least two or three working days; hence, the latest UT 1 data are rarely less than two days old, and are often a week or more old for some measurement services. Because of this delay, even real-time estimates of UT 1 are potentially in error by an amount exceeding the DSN requirements. Consequently, two different tacks are being pursued at JPL to improve the accuracy of estimates and predictions of UT1: 1) more timely data, and 2) improved prediction schemes. The work reported here deals with the incorporation of axial atmospheric angular momentum (AAM) analysis data and AAM forecast data into the JPL Kalman Filter as a proxy for LOD; the former are the timeliest data currently available, while the latter represent a prediction of LOD based on physical, rather than stochastic, models.

Fluctuations in Earth rotation over time scales of less than a few years are dominated by atmospheric effects, and numerous studies have demonstrated the high correlation between LOD and AAM at these periods [Rosen and Salstein, 1983; Eubanks et al., 1985; Hide and Dickey, 1991, for example]. Several meteorological centers engaged in operational weather forecasting generate both near-real-time estimates of A AM and intermediate-range forecasts of AAM. Studies by Rosen et al, [1987; 1991] (see also Bell et al, [1991]) have demonstrated that these AAM forecasts can be skillful indicators of AAM (relative to simple statistical predictors) out to several days. Whereas AAM analysis values are generated from contemporaneous meteorological measurements and thus represent a current estimate of atmospheric angular momentum, AAM forecast values represent estimates of the global atmospheric angular momentum at a future epoch based on physical models, and thus can be

used to estimate future values of LOD. Our approach is to utilize these AAM analysis and forecast data as proxy data sets for LOD, to be relied on primarily when geodetic data are infrequent or no longer available.

The data types, both geodetic and meteorological, that are employed in the JPL filter, along with stochastic models for the behavior of both LOD and AAM, are discussed below in section 2, Section 3 describes the implementation and functioning of the **JPL Kalman** Filter, henceforth referred to as KEOF (the **Kalman** Earth Orientation Filter). Section 4 deals with the accuracy of predictions of LOD and UT1 that emerge from KEOF, and their improvement when AAM analysis and forecast data are incorporated into the filtering scheme. Section 5 discusses additional difficulties with UT1 estimation and proposes some future improvements in the filtering and prediction strategies.

2. The Measurement Data

In the optimal combination of diverse data types to form a best estimate of UT1, a number of factors must be dealt with explicitly. These include the accuracy and precision of the various data sets, the variable interval between measurements, that component or linear combination of components of Earth orientation which a particular technique actually measures, and any inter-series biases or trends. These considerations, as well as the need to accurately model the growth in Earth orientation uncertainty in the absence of measurements, motivated the design and implementation of the **JPL Kalman** Filter.

For near-real-time operational estimates of UT1, only those high-precision data types, both geodetic and meteorological, that are available in a timely fashion are used in **KEOF**. Table 1 summarizes the characteristics of these various data sets, which are described more fully below; additional information may be found in **IERS [1992a; 1992b]**.

Table 1
near
here

Geodetic Data

Three modern high-precision techniques have been used over the past decade to monitor Earth orientation: Very long baseline **interferometry (VLBI)**, satellite laser ranging

(SLR), and lunar laser ranging (LLR). All three techniques are capable of milliarcsecond-level determination of various components of Earth orientation. Five services provide the geodetic data used in this study: (1) The National Oceanic and Atmospheric Administration's (NOAA) Laboratory for Geosciences provides single-baseline VLBI measurements of UT1-UTC daily, and multiple-baseline VLBI UT1 and Polar Motion (UTPM) estimates every five-to-seven days through the IRIS (International Radio Interferometric Surveying) program. These are known as the IRIS intensive and IRIS multibaseline data sets, respectively. (2) The NAVNET VLBI program of the U. S. Naval Observatory (USNO) produces multibaseline UTPM data weekly, staggered in time with those of the IRIS multibaseline network. JPL provides both (3) VLBI measurements of Earth orientation through its TEMPO (Time and Earth Motion Precision Observations) program roughly twice a week, and (4) LLR Earth orientation measurements at irregular intervals. (5) The Center for Space Research (CSR) of the University of Texas at Austin provides SLR measurements of polar motion and UT 1 at roughly three-day intervals.

The IRIS and NAVNET VLBI data and the CSR SLR data used operationally in KEOF are distributed weekly by their respective organizations, usually on Wednesdays to facilitate their use by the International Earth Rotation Service (IERS) Rapid Service. In each delivery, the most recent IRIS data are typically ten days to two weeks old, the most recent NAVNET data are typically six to ten days old, and the most recent SLR data are typically three to five days old. Thus, on any given day, the most recent data available from these services may be up to 7 days older than these values. The TEMPO data are reduced at JPL and are made available to KEOF as soon as processing is complete. When conditions are ideal, 24-hour turnaround can be achieved, although two or three day delays are more typical [Steppe et al., 1992b]. LLR data are also reduced at JPL and solutions can be obtained in under a day, but these measurements are collected and processed in a less frequent, non-operational mode.

The formal errors assigned to the UT1 measurements differ considerably among techniques [IERS, 1992b]. IRIS multi baseline data typically have the smallest formal errors; for recent data, these range from 0.015 to 0.020 ms. There is evidence, however, that these numbers are overly optimistic, and that more realistic error estimates are up to one and a half times the formal errors [Gross, 1992; IERS, 1992a]. NAVNET formal errors are also quite low, ranging from 0.015 to 0.025 ms for recent data, but these values may also need to be inflated by up to 30%. In contrast, the IRIS intensive and SLR UT1 values possess formal errors ranging from 0.04 to 0.10 ms. (Note, however, that SLR UT 1 data are not used in the operational filter. SLR UT 1 data are tied to an independent UT 1 solution at long periods to correct for satellite node effects and thus do not constitute a truly independent data set [Eanes and Watkins, 1992]. For this and other reasons, only SLR polar motion data are used by KEOF.) TEMPO and LLR do not estimate UT1 directly, but instead sense those components of Earth orientation that can be measured from one baseline or site. For TEMPO VLBI, these are the components of Earth orientation orthogonal to rotations about the VLBI baseline (transverse and vertical, or equivalently, UTO and variation of latitude), while for LLR, the measured quantities are UTO and variation of latitude [Lambeck, 1988; Steppe et al., 1992b; Grosset al., 1993]. Formal errors in these components typically range (in time units) from 0.02 to 0.20 ms for TEMPO and from 0.03 to 0.30 ms for LLR.

Atmospheric Data

Estimates of the **total** angular momentum of the atmosphere about the polar axis are routinely available from a number of meteorological centers engaged in real-time weather prediction. These estimates are a product of operational global numerical weather forecasting models in which numerous atmospheric parameters, such as wind, pressure, and temperature fields, are continuously being updated as large quantities of in situ and remotely sensed meteorological data are assimilated into the model. Since these models are used to generate ongoing weather forecasts for immediate distribution, the AAM values themselves are also available with little delay. The U. S. National Meteorological Center (NMC), the United

Kingdom Meteorological Office (UKMO), the European Center for Medium-Range Weather Forecasts (ECMWF), and the Japanese Meteorological Agency (JMA) all produce estimates of various AAM components every 12 or 24 hours. In addition, the NMC, UKMO, and ECMWF utilize their models to predict the values of atmospheric quantities up to 10 days in the future. These predictions are based on the current state of the atmosphere (after all extant data have been assimilated into the model) propagated into the future taking into account as many physical processes as is computationally feasible. Those AAM estimates that incorporate raw meteorological data obtained up to and beyond the epoch of the estimate are known as AAM analysis values. Those AAM estimates made without any data yet available at the epoch of the estimate are known as AAM forecast (AAMF) values.

Several sources of error affect all meteorological estimates of AAM. These include limited geographic data coverage, finite atmospheric model thickness, and physical and numerical model approximations. Raw meteorological data are gathered unevenly, with the densest coverage available in the northern hemisphere and over continents. Large areas of the southern hemisphere are without in situ data, as are upper levels of the atmosphere in the tropics. Although these regions are being monitored through remotely sensed data from weather satellites, the computed wind and pressure fields in these areas are more model dependent since in situ data are lacking. Atmospheric models extend up to a small but non-zero top pressure level, effectively excluding a portion of the stratosphere when computing the atmospheric angular momentum. This can generate errors in AAM estimates of up to 10% on annual time scales [Rosen and Salstein, 1985]. As dynamical forecasts of the atmosphere are extremely sensitive to both model errors and small errors in the initial conditions, errors in forecasting increase rapidly as the forecast interval grows, and all forecast ability is lost after about 2 weeks [Rosen et al., 1987 b].

In the normal operation of KEOF, the AAM and AAMF series produced by the NMC are employed. Unlike the AAM data products of the other centers, the NMC data have been available since 1985 on a daily basis by dialing up an NMC computer and transferring the

data via modem. The other centers have not, until recently, had such a real-time capability. Use of data from these other centers in routine KEOF operations is under investigation, and preliminary results have been reported elsewhere [Freedman and Dickey, 1991].

None of the centers that compute AAM include uncertainty estimates with their distributed AAM values. The JPL **Kalman** Filter requires realistic formal errors for all input data types, however, including AAM. A number of studies have been performed to assess the errors present in the AAM data [Rosen et al., 1987a; Gross and Eubanks, 1988; Bell et al., 1991; Gross et al., 1991]. These have primarily involved intercomparisons of the AAM time series of the various centers with each other and with **LOD**. From these and our own studies, a nominal value of 0.05 ms has been chosen as the formal error for both the NMC AAM analysis and forecast series. This nominal value is consistent with the RMS difference between AAM series from different centers, but it effectively assumes an error structure for the AAM that is **uncorrelated** in time. A recent study by Dickey et al. [1992] has shown that the inter-center differences are, in fact, correlated over time, which suggests that a substantially smaller white-noise formal error for the AAM data may be adequate, an option that is currently under investigation. Ideally, we would like to obtain formal errors for each data point directly from the numerical models of the meteorological centers, but in practice such estimates are difficult, especially if the errors are correlated over time.

The AAM and AAMF values used in KEOF are derived from the angular momentum of the **zonally** averaged **zonal** winds (the “wind” term), according to

$$M_w(p_u) = \frac{-2\pi a^3}{g} \int_{p_s}^{p_u} \int_{-\pi/2}^{\pi/2} [u] \cos^2 \phi \, d\phi \, dp \quad (2)$$

where M_w is the AAM from the wind term, a is the mean radius of the Earth, g is the acceleration of gravity, $[u](\phi, p)$ is the **zonal** mean **zonal** wind (the eastward component of wind averaged over all longitudes in a particular band of latitudes and heights), ϕ is the latitude, and p is the pressure level of the atmosphere, ranging from surface pressure ($p_s = 1000 \text{ mb}$) to the upper pressure limit defining the top of the model (p_u) [Rosen and Salstein, 1983;

Eubanks et al., 1985]. For the NMC data used in KEOF, the upper pressure level is $p_u = 100$ mb; hence, the top 10% of the atmosphere is ignored, and no attempt is currently made in operational KEOF processing to correct for this missing portion of the atmosphere. Also ignored are the effects on the total AAM of variations in atmospheric pressure (the “pressure” or “matter” term). The exclusion of the stratosphere and pressure term is a result of the historical development of the AAM data product distributed by the NMC. The early AAM and AAMF estimates were only available for the wind term computed up to 100 mb. Because a continuous data set is desirable for operational KEOF stability, this is the data set still in operational use. Portions of the stratosphere (up to $p_u = 50$ mb) and the AAM pressure term are available from the NMC for more recent data, and their use is currently under study. The net effect of these two error sources is probably less than 20%.

Relationship Between AAM and LOD

Assuming the total angular momentum of the Earth as a whole to be conserved (i.e., ignoring external torques), if the solid Earth experiences a change in its angular momentum, this momentum must be **transferred** to or from another component of the Earth, such as the atmosphere, ocean, or liquid core. Over **decadal** time scales, the Earth’s liquid core is thought to play a significant role in this momentum exchange, but at time scales of a few years (**interannual**) and less, the atmosphere is expected to play the dominant role. As mentioned above, the high correlation between LOD and AAM at **interannual** and shorter periods has been demonstrated by many studies over the past decade [e.g., Hide et al., 1980; Rosen and Salstein, 1983; Eubanks et al., 1985; Morgan et al., 1985; Rosen et al., 1990; Dickey et al., 1992]. Significant coherence is found between the two time series at periods down to 8 days, with lack of coherence at shorter periods apparently due to the declining **signal-to-measurement** noise ratios of the data sets [Dickey et al., 1992]. Other possible locations for momentum storage, such as the oceans, appear to play a minor role over these time scales.

Assuming that the solid Earth exchanges angular momentum only with the atmosphere and that the moment of inertia of the solid Earth remains constant, AAM and LOD are related according to

$$\Delta A = \frac{A_0}{\Omega C_m} \Delta M_w = (1.67 \times 10^{-29} \text{ s}^2/\text{kg m}^2) \Delta M_w \quad (3)$$

where Ω is the average angular rotation rate of the Earth and C_m is the polar moment of inertia of the solid Earth (crust and mantle) [Rosen and Salstein, 1983; Eubanks et al., 1985]. AAM is usually presented in time units using the conversion factor given in Eq. (3) (where the values $\Omega = 7.292 \times 10^{-5} \text{ s}^{-1}$ and $C_m = 7.10 \times 10^{37} \text{ kg m}^2$ have been employed [Eubanks et al., 1985; Lambeck, 1988]).

The close relationship between AAM and LOD can be seen in Figure 1. Figure 1a displays a two-year time series of LOD (with a long-term trend and tidal lines removed) together with that of the AAM wind term. Note the strong similarities between the two curves. This is shown more concretely in the coherence plot of Figure 1b (after Dickey et al., [1992]), where the agreement between the two time series is significant down to about 8 days.

**Fig. 1a
and 1b
near
here**

Since high coherence exists between AAM and LOD at periods greater than about 10 days, and both AAM and LOD exhibit substantial power at these longer periods (as seen in the power spectral density plots described below), it is reasonable to employ AAM data as a proxy for LOD when geodetic data are lacking. At shorter periods, Dickey et al. [1992] conclude that the signal-to-noise ratio of the AAM is superior to that of the LOD, suggesting that the AAM data may even provide a better indication of the high-frequency variability of true LOD than do the geodetic measurements of UT 1 (assuming no other reservoir for angular momentum storage). Thus, unless improvements in either geodetic or atmospheric data sets suggest otherwise, AAM is both a reasonable proxy and useful supplement to geodetically derived LOD even for high-frequency fluctuations.

When LOD variations are largest in magnitude, AAM could be especially important for LOD and UT1 prediction. As seen in Fig. 1a, there are episodes of large and rapid LOD change which are promptly and accurately matched by similar AAM variations. Since the geodetic measurements that monitor these fluctuations often take several days to process, the near-real-time AAM data can quickly capture this variability, and thus aid in predicting UT1 during these critical events.

In order to implement the Kalman filtering scheme described in the next section, we need to develop stochastic models for the behavior of LOD, AAM analyses, AAM forecasts, and their differences (e.g., AAM – LOD, AAMF – AAM, etc.). Eubanks et al. [1985] investigated the relationship between the AAM and LOD data available in the early 1980's, concluding that both AAM and LOD behave as random walk processes with the difference between them also behaving as a random walk with about 1/10 the power of either AAM or LOD individually. Later work by Eubanks et al. [1987] examined AAM forecasts, and proposed an autoregressive model for the AAM forecast errors. These results are illustrated in Figure 2, using operational NMC AAM analysis and forecast data from 1987.0 to 1991.0 and a time series of LOD data generated by KEOF from the various geodetic data sets described above. The stochastic models are formulated by careful analyses of figures such as these, with an emphasis on capturing as accurately as possible the behavior of the modeled quantities both around the frequencies where measurement noise begins to corrupt the true signal and at those periods most relevant for short-term UT1 prediction (5-20 days). Thus, spectral models of the various noise components present in the data are also important [Eubanks et al., 1985; Dickey et al., 1992].

Fig. 2a
and 2b
near
here

As seen in Figure 2a, the AAM and LOD time series possess power spectra that follow an f^{-2} curve across a broad range of frequencies, f , indicative of random walk behavior. The power spectral density (PSD) of the white-noise stochastic process forcing the random walk model for LOD is $0.0036 \text{ ms}^2/\text{day}$. The power spectrum of the difference series between LOD and AAM also approximately follows an f^{-2} curve, with a much smaller

white-noise PSD forcing of 0,0004 ms²/day. Figure 2b shows a similar comparison between the AAM analysis and 5-day forecast power spectra, Here, the difference is less like a random walk, and can be better modeled by a first-order autoregressive process, In addition, there is an empirically-measured bias between the AAM and AAMF time series that varies with the AAMF forecast interval. These stochastic behaviors are incorporated into the JPL Kalman Filter models described below,

3. KEOF Implementation

The JPL Kalman Earth Orientation Filter (KEOF) is a state-space, time-domain, optimal linear filter [Gelb, 1974, for example]. Its purpose, structure, and implementation are summarized in Morabito et al. [1988]. What will be described below is the general implementation within KEOF of geodetic data types, and the detailed implementation of AAM analysis and forecast data types.

State Equations

The linear stochastic model used to derive the filter can be described by:

$$\frac{d\mathbf{x}}{dt} = \mathbf{F} \mathbf{x} + \boldsymbol{\omega} \quad (4)$$

where \mathbf{x} is the state vector containing all relevant components, \mathbf{F} is a constant coefficient matrix describing the dynamics of the system, and $\boldsymbol{\omega}$ is a white-noise, zero-mean stochastic process vector, whose elements are statistically independent of one another. The state and white noise vectors consist of the following:

Table 2
near
here

$$\begin{aligned} \mathbf{X}^T &= (X \ Y \ \mu_1 \ \mu_2 \ S \ \dot{S} \ U \ L \ \mu_A^b \ \mu_F) \\ \boldsymbol{\omega}^T &= (0 \ 0 \ \omega_1 \ \omega_2 \ 0 \ \omega_S \ 0 \ \omega_L \ \omega_A^0 \ \omega_F) \end{aligned} \quad (5)$$

where all the variables are defined in Table 2 and the superscript “T” denotes the vector transpose. The first 6 elements of these vectors relate to polar motion measurement and modeling. They are described in Morabito et al, [1988] and will not be dealt with further

here, The last five elements describe the interrelationships among UT1, LOD, AAM analysis, and AAM forecast data. Although they are dynamically separable from the polar motion components, these five elements are not independent of the first six elements in practice because certain geodetic data types do not measure UT1 independently of X and Y. TEMPO and LLR, for example, sense components of Earth orientation (e.g., UTO, variation of latitude) which are linear combinations of polar motion and UT1, while the multibaseline NAVNET data possess full covariance matrices that relate UT and polar motion. Hence, in practice, all eleven state vector components are, to some extent, correlated with each other.

Matrix F incorporates the relationship among the various state vector components. The relationship between UT1 (U) and LOD (A) as modeled within the filter is:

$$\frac{dU}{dt} = -L \quad (6)$$

$$\frac{dL}{dt} = \omega_L \quad (7)$$

where $L \equiv A/\Lambda_0$ with units of milliseconds per day represents a normalized form of LOD. Since ω_L represents a white-noise stochastic process, L behaves as a random walk (integrated white noise) while U is modeled as an integrated random walk, Equation (6) is a restatement of the definition of LOD (1) in terms of L . (If t is given in days, $\Lambda_0 = 1$ and the magnitudes of A and L are equal.) Equation (7) emerges from Figure 2a and studies such as Eubanks et al. [1985] and Dickey et al. [1992], wherein the LOD, with tidal terms removed, appears to behave as a random walk over a broad range of frequencies. The AAM analysis (A) component is described by:

$$A = L + \mu_A \quad (8)$$

$$\frac{d\mu_A}{dt} = \omega_A \quad (9)$$

where AAM differs from LOD by a difference term, μ_A , that also behaves as a random walk but with a much smaller variance, as suggested by Figure 2a. Note that A is also normalized

($A \equiv \text{AAM}/\text{Ao}$) to be consistent with the definition of L , AAM forecast values ($F \equiv \text{AAMF}/\text{Ao}$) are modeled by:

$$F = A + \mu_F + b \quad (10)$$

$$\frac{d\mu_F}{dt} = -\frac{\mu_F}{\tau_i} + \omega_F \quad (11)$$

The AAM forecasts are treated as the sum of the true AAM, a constant bias term b , and an exponentially decaying term μ_F excited by white noise. Equation (11) describes a simple first-order autoregressive model which follows the curve shown in Figure 2b reasonably well. The exponential time constant is τ_i , determined empirically to be on the order of a few days. For routine filter operation, τ_i is usually set to the AAM forecast lead time [Eubanks et al., 1987]. Since the stochastic processes ω_L , ω_A , and ω_F are independent, the state-vector quantities that they drive, L , μ_A , and μ_F , as modeled above are also independent, Estimates of these quantities in the presence of data, however, are highly interdependent.

It should be emphasized that these stochastic models, and especially the model parameter values themselves, are empirically determined and are a function of the data sets employed. Hence, the models and parameter values need to be periodically reexamined and adjusted as the data sets improve. The parameter values currently used in operational KEOF processing are listed in Table 3, where Q represents the power spectral density of the zero mean, white noise process ω .

Table 3
near
here

Forward Kalman Filtering

The solution to equation (4) is given by

$$\mathbf{x}(t) = \Phi(t - t_0) \mathbf{x}(t_0) + \int_{t_0}^t \Phi(t - \eta) \omega(\eta) d\eta \quad (12)$$

where $\Phi(\Delta t)$ is known as the transition matrix and can be expressed as an exponential

$$\Phi(\Delta t) = \exp(F \Delta t) = \sum_{k=0}^{\infty} \frac{F^k \Delta t^k}{k!} \quad (13)$$

Equation (12) describes the evolution of the state vector with time, given the “system model” for a Kalman optimal linear filter shown in (4) [e.g., Gelb, 1974]. The best estimate, $\hat{\mathbf{x}}_i$, of this state vector at time t_i , in the absence of new measurements, is given by the propagated Kalman state estimate

$$\hat{\mathbf{x}}_i = \Phi(t_i - t_{i-1}) \hat{\mathbf{x}}_{i-1} \quad (14)$$

for $t_{i-1} < t_i$. This estimate is not affected by process noise but is a result solely of a deterministic model applied to the previous state estimate. The corresponding propagated state error covariance matrix is

$$P_i = \Phi(t_i - t_{i-1}) \hat{P}_{i-1} \Phi^T(t_i - t_{i-1}) + \int_{t_{i-1}}^{t_i} \Phi(t_i - \eta) Q \Phi^T(t_i - \eta) d\eta \quad (15)$$

where Q is the process noise matrix (a diagonal matrix with elements Q_i). The state covariance matrix P_i includes both the effect of propagating the previous state error forward in time (the first term on the right hand side of (15)) and the effect of adding process noise (the second term), Appendix A contains the derivation of (13) and the evaluation of (15) for the lower half of the state vector.

Ignoring polar motion components, (14) reduces to the following set of equations

$$\begin{aligned} V_i &= U_{i-1} - \Delta t L_{i-1} \\ L_i &= L_{i-1} \\ \mu_A &= \mu_{A, i-1} \\ b_i &= b_{i-1} \\ \mu_{Fi} &= \mu_{Fi-1} \exp(-\Delta t / \tau_i) \end{aligned} \quad (16)$$

where $\Delta t = t_i - t_{i-1}$. Thus, in the absence of new data, the state vector components L , μ_A , and b remain constant, while U and μ_F behave as linear and exponentially damped quantities, respectively. The effect of the exponential damping on μ_F is that as Δt grows large, μ_F approaches zero, and the best estimate of the AAM forecast becomes simply the AAM analysis value plus a bias, i.e., $F \rightarrow A + b$.

Measurements are modeled as

$$z(f) = \mathbf{H}\mathbf{x}(t) + \mathbf{V}(t) \quad (17)$$

where z is the measurement vector or scalar at time t , v is the measurement noise vector or scalar (**assumed** to be white with zero mean), and H is the design matrix relating the state vector to the measurements

$$H^T = (\mathbf{h}_x \ \mathbf{h}_y \ \mathbf{h}_u \ \mathbf{h}_A \ \mathbf{h}_F) \quad (18)$$

The h vectors are trivial for PMX, PMY, and UT1, and can be derived for AAM and AAMF measurement types from equations (8) and (10). The latter three h vectors are thus

$$\begin{aligned} \mathbf{h}_u^T &= (0 \ 0 \ 0 \ 0 \ 0 \ 0 \ 1 \ 0 \ 0 \ 0 \ 0) \\ \mathbf{h}_A^T &= (0 \ 0 \ 0 \ 0 \ 0 \ 0 \ 0 \ 1 \ 1 \ 0 \ 0) \\ \mathbf{h}_F^T &= (0 \ 0 \ 0 \ 0 \ 0 \ 0 \ 0 \ 1 \ 1 \ 1 \ 1) \end{aligned} \quad (19)$$

As measurements are collected, the state vector and state covariance matrix must be updated to include the new data. The updated state estimate, essentially a weighted average of the state and measurement vectors, is

$$\hat{\mathbf{x}}_+ = (\hat{\mathbf{P}}_-^{-1} + \mathbf{H}^T \mathbf{R}^{-1} \mathbf{H})^{-1} [\hat{\mathbf{P}}_-^{-1} \hat{\mathbf{x}}_- + \mathbf{H}^T \mathbf{R}^{-1} \mathbf{z}] = \hat{\mathbf{x}}_- + \hat{\mathbf{P}}_+ \mathbf{H}^T \mathbf{R}^{-1} [\mathbf{z} - \mathbf{H} \hat{\mathbf{x}}_-] \quad (20)$$

where the “-” and “+” subscripts refer to quantities preceding and following, respectively, an update with the new measurement z , R is the measurement error covariance matrix, and $\hat{\mathbf{P}}_+$ is the updated state covariance matrix

$$\hat{\mathbf{P}}_+ = (\hat{\mathbf{P}}_-^{-1} + \mathbf{H}^T \mathbf{R}^{-1} \mathbf{H})^{-1} \quad (21)$$

Equations 20 and 21 are usually represented in a modified form for Kalman filtering using the Kalman gain matrix K [Gelb, 1974]:

$$\hat{\mathbf{x}}_+ = \hat{\mathbf{x}}_- + \mathbf{K} [\mathbf{z} - \mathbf{H} \hat{\mathbf{x}}_-] \quad (22a)$$

$$\hat{\mathbf{P}}_+ = [\mathbf{I} - \mathbf{K} \mathbf{H}] \hat{\mathbf{P}}_- \quad (22b)$$

$$\mathbf{K} = \hat{\mathbf{P}}_- \mathbf{H}^T [\mathbf{H} \hat{\mathbf{P}}_- \mathbf{H}^T + \mathbf{R}]^{-1} \quad (22c)$$

Although this description is computationally more efficient than that described by (20) and (21) since one matrix inversion is required rather than three and the dimension of that one matrix is lower, “for the specific application discussed here, (22) is not ideal. The

measurement covariance matrix R for certain geodetic data types may contain elements with essentially infinite (i.e., unknown) values [Steppe et al., 1992a, for example]; such an error structure is better represented by the inverse covariance matrix R^{-1} , known as the information matrix. Because the state vector contains only 11 components, the computational work involved in performing the additional matrix inversions does not significantly hinder operation of the filter.

Filtering in KEOF is a multi-step process. The state vector and state covariance matrix are first initialized with a reasonable set of a priori values. These values are chosen such that the state vector values will be close to the empirical values at the epoch that filtering begins and the diagonal state covariance matrix will have elements sufficiently large to allow the a priori state vector to quickly converge to the empirical value when measurements become available. The state vector and covariance matrix are then propagated using (14) and (15) to the next event time. This event may be either a print time or a measurement epoch. At a print time, the current state vector and covariance matrix are written to an output file. If the event is a new measurement, a data update is performed using (20) and (21). Additional updates occur if other measurements exist at that epoch, otherwise the filter propagates to the next event. If the print time and data epoch are simultaneous (to within a small fraction of a day), the data update is performed before the state vector and covariance matrix are output.

During the propagation process, stochastic excitation adds uncertainty to the state covariance matrix. According to the model developed in Appendix A, if the state were known exactly at time $t = 0$, the one-sigma error estimates would grow with time as follows (with t measured in days):

$$\begin{aligned}
 \sigma_U &= 0.0351\% \text{ ms} \\
 \sigma_L &= 0.060 \, t^{1/2} \text{ ms / day} \\
 \sigma_{\mu_A} &= 0.020 \, t^{1/2} \text{ ms / day} \\
 \sigma_b &= 0 \text{ ms / day} \\
 \sigma_F &= 0.075 [1 - \exp(-0.4t)]^{1/2} \text{ ms / day} \approx \begin{cases} 0.047 \, t^{1/2} \text{ ms / day} & (\text{for } t \text{ small}) \\ 0.075 \text{ ms / day} & (\text{for } t \text{ large}) \end{cases}
 \end{aligned} \tag{23}$$

Thus, modeled UT1 error estimates grow as $t^{3/2}$, increasing very quickly for times longer than a day or so, while modeled LOD, AAM, and AAMF uncertainties grow as $t^{1/2}$, quickly at first but less rapidly after a few days. The result in (23) implies that if UT 1 and LOD were known perfectly at some moment, then, in the absence of additional data, the uncertainty in the predicted value of UT 1 would exceed the current DSN UT 1 requirement of 0.6 ms after about 6.5 days.

Backward Kalman Filtering and Smoothing

For prediction of Earth orientation components, the **Kalman** filter need only be run in the forward direction, i.e., by assimilating data in chronological order, using stochastic models to extrapolate the series forward in time. To create an optimal smoothing, the **Kalman** filter must also be run in reverse chronological order; this “backward” time series is then vector weighted averaged with the “forward” time series on a point by point basis to generate an optimally smoothed estimate at each output time point. In this averaging scheme, care must be taken that input data are not used twice in the estimate. Thus, if a measurement at some epoch has already been used in forward filtering to produce an estimate at that epoch, the backward filtering must output an estimate for that epoch prior to assimilating the **measurement**. In backwards filtering, therefore, when a print time and data update time coincide, the output is generated before any measurements at that time are used to update the state.

A number of modifications occur to the **Kalman** filtering scheme in backward filtering. Although all the data update equations remain the same (17-22), the propagation equations change slightly. These changes are discussed in Appendix B. The most obvious is the change in the modeled estimate and propagated uncertainty of the μ_F component. Applying (B5) to (B3), the propagated estimate of μ_F is

$$\mu_{Fi} = \mu_{Fi-1} \exp(|\Delta t|/\tau_i) \quad (24)$$

which grows exponentially large as Δt increases. The portion of the propagated μ_F uncertainty due to process noise (B7) is

$$\sigma_F = 0.075 [\exp(0.4t) - 1]^{1/2} \text{ ms / day} = \begin{cases} 0.047 t^{1/2} \text{ ms / day (for small } t) \\ \rightarrow \infty \text{ (for } t \text{ large)} \end{cases} \quad (25)$$

while the error propagated from the previous estimate (B6) also grows as $[\exp(0.4t)]^{1/2}$. In contrast with forward filtering, the μ_F estimates and uncertainties in the backwards filter will grow exponentially large over time without AAMF data to constrain them to finite values. The computational problems due to such large numbers are overcome in practice (if, for example, forecast data are not used) by setting the time constant τ_i to a large value.

The smoothed series is a weighted average of the forward and backward filterings. Thus

$$\hat{\mathbf{x}}_{\text{smoothed}} = (\hat{\mathbf{P}}_f^{-1} + \hat{\mathbf{P}}_b^{-1})^{-1} [\hat{\mathbf{P}}_f^{-1} \hat{\mathbf{x}}_f + \hat{\mathbf{P}}_b^{-1} \hat{\mathbf{x}}_b] \quad (26a)$$

$$\hat{\mathbf{P}}_{\text{smoothed}} = (\hat{\mathbf{P}}_f^{-1} + \hat{\mathbf{P}}_b^{-1})^{-1} \quad (26b)$$

where the “f” and “b” subscripts refer to the forward and backward filter output, respectively.

Filtering Examples

The portion of the Kalman filter designed to deal with UT1 and LOD incorporates information from three raw data types—geodetic UT1 and meteorological AAM analysis and forecast data—within five state vector components: U , L , μ_A , b , and μ_F . Having described the models for these components within KEOF, it is illustrative to examine how the input data are dealt with in practice by the filter. Two different sets of examples are presented below. In the first, synthetic sets of data are used as UT1, AAM, and AAMF input data. These three data sets are formed using simple analytic functions, chosen to highlight the influence on the filtered output quantities of each individual data set. The second set of examples uses true geodetic and atmospheric data to qualitatively illustrate the filtering and smoothing performed by KEOF.

**Fig. 3
near
here**

Figure 3 shows the three synthetic raw data sets used in the **first** example, together with their defining expressions. The UT1 (Fig. 3a), with a one-sigma formal error of 0.02 ms, varies linearly with time, the AAM analysis series (Fig. 3b) consists of a bias term

and a slowly varying sinusoid (with $\sigma = 0,05$ ms), while the AAM forecast data (Fig. 3b) are similar to the AAM analysis data but differ by a small bias term and an additional low-amplitude, high-frequency sinusoid. All data sets contain points with daily spacing. To illustrate the effects on the filtered solution of the addition and deletion of the various data types, the data sets are staggered in time such that the UT1 data begin on January 1 and end on August 31, the AAM analysis data begin and end two months later (March 1 and October 31, respectively), and the AAM forecast data, two months later still (May 1 and December 31; since these are five-day forecasts, however, their time tags actually run from May 6 to January 5).

**Fig. 4a
and 4b
near
here**

The smoothed estimates and formal errors for UT1, LOD, AAM, and AAMF generated by KEOF are shown in Figure 4. The smoothed UT1 series (Fig. 4a) accurately reflects the input UT1 data until September when the raw data cease. The UT1 behavior is subsequently governed by the filter's estimate of integrated LOD, which, in turn, is now controlled by the AAM analysis and forecast data. The UT1 formal errors (Fig. 4b) reflect this changeover, and increase by 3 orders of magnitude over the final four months due to the stochastic model's estimate of the growth in uncertainty of μ_A and L .

**Fig. 4c
and 4d
near
here**

The estimated LOD and its formal error (Figs. 4c and 4d) remain fairly smooth over the time interval in which the geodetic UT1 data are available and are only perturbed slightly by the addition of the atmospheric data sets in March and May, but the subsequent LOD behavior after the geodetic data are exhausted is closely controlled by the atmospheric data. The filtered values for the atmospheric time series (Fig. 4c) agree well with their corresponding raw data sets when these data are available, but are controlled by the most closely related existing data at other times. For example, in the first two months when geodetic data alone are available, both atmospheric quantities behave similarly to LOD, albeit with a constant offset, while in November and December when only AAMF data exist, both LOD and AAM estimates incorporate the high-frequency structure of the AAMF series. The formal errors (Fig. 4d) successfully reflect the amount and type of raw data going into the estimates for each component, however, with the errors dropping as more closely-related data types

become available and rising as these data cease. If no raw data are available (see the last two months in Fig. 4), the estimated quantities and their uncertainties vary according to the stochastic propagation models described above.

Figure 4 illustrates the properties desired for a sensible combination of geodetic and atmospheric data types. When geodetic data are available, the smoothed geodetic series is consistent with these data, even if concurrent atmospheric data behave inconsistently. When geodetic data are not available, the geodetic parameter estimates are controlled by whatever data types do exist, namely, the atmospheric data.

In the second example of KEOF performance, a set of real geodetic and atmospheric data (as listed in Table 1) were employed. These were operational data sets, in that they were adjusted according to the following procedure. Prior to filtering the data, the various geodetic data sets were compared with a reference UTPM time series aligned with that of the IERS [Gross, 1992; IERS, 1992a]. A bias and rate were removed from each time series to render them consistent *in* their long-term behavior with the reference series. In addition, the formal errors of each geodetic data set were adjusted so that the normalized **chi-squared** value of the data residuals with respect to a smoothing incorporating **all** other data sets was near to unity [Sung, 1992]. The formal errors of the atmospheric data are assumed to be 0.05 ms, as explained above.

Fig. 5
near
here

A number of characteristics of the KEOF filtering and smoothing of the raw data are illustrated in Figure 5, where the residuals of the input data with respect to the smoothed KEOF output are shown for the UT1 component, together with the formal errors on both the input data and smoothed output. Only the IRIS and NAVNET VLBI data are shown, since only these series report UT 1 values which are used by KEOF directly. The RMS scatter of the data residuals is comparable in size to the formal error of the input data, indicating that the smoothed values generally lie within the one-sigma error bars of the raw data. For the UT1 component, the formal error of the smoothed series is about half that of the best-quality measurement data input into the filter. Note that the relative values of input formal error,

smoothed formal error, and the raw-minus-smoothed residual are variable and depend on data type, data spacing, stochastic model parameters, and other characteristics of the data and model.

Although the primary purpose of incorporating atmospheric data into the filter is to improve predictions of UT1 and LOD when geodetic data are absent, the addition of AAM and AAMF data affects the estimates of UT1 and LOD even when geodetic data are present. To ascertain whether this effect is significant in practice, two filter runs were performed, one using only geodetic data, the other with both AAM and AAMF data sets included. The differences between the filtered estimates for both the UT1 and LOD components are shown in Figure 6. Also shown are the formal errors for these components from the **geodetic-plus-atmospheric-data** filter run. (Note that the formal errors from this run are always less than the formal errors for the geodetic-data-only run, since additional data can only add strength to the smoothed solution.) The differences between the two filter estimates are, for the most part, less than 0.04 ms in magnitude for UT1 and 0.03 ms for LOD, with RMS scatter of 0.019 ms and 0.011 ms, respectively. These differences are within the one-sigma formal error bars (± 0.04 ms) of the estimates. Thus, UT1 and LOD series generated with AAM data are among the family of solutions permitted by the series generated without AAM data, and vice versa.

**Fig. 6
near
here**

The differences between the two series will increase if the formal errors of the input atmospheric data are reduced, since the AAM would then have a stronger influence on the LOD estimates. Tests with the AAM input formal error set at $\sigma = 0.005$ ms still yield RMS scatters of 0.03 ms and 0.02 ms for UT1 and LOD, respectively, comparable to the one-sigma output formal error of 0.03 ms. Hence, adding AAM and AAMF data to an already dense mix of geodetic data does not affect the resulting filtered UT 1 and LOD solutions to a statistically significant degree; these data types only play a prominent role when the geodetic data become sparse or significantly degraded in quality.

4. UT1 and **LOD** Prediction

Since the original goal of incorporating AAM as a data type was to aid in the prediction of UT1, the ultimate test of our method is whether AAM analysis and forecast data do indeed improve real-time prediction. Two methods are being used to evaluate the effectiveness of including AAM data. One method is to perform periodic spot checks of the operational predictions by estimating and predicting UT1 both with and without the AAM data. The other method uses a version of the filter that automatically performs a set of case studies to examine the effects of including AAM data for a large number of filter predictions. Since this latter method yields more reliable statistics, results obtained from a set of simulated operational filter runs are shown below.

The version of the **Kalman** filter that performed this work has been described in Freedman and Dickey [199 1]. It uses the same smoothing and prediction algorithms as **KEOF**, but automatically splits up a long time series of data into equal length subsets to use to predict UT1. The result is a series of predictions that simulate the operational functioning of the filter. A reference “truth” series is also generated, and the prediction and reference series are difference. The resulting series of prediction errors are combined to yield an estimate of the prediction error magnitude as a function of time since the filtering epoch.

Fig. 7
near
here

The procedure for generating these case studies is shown schematically in Figure 7. The reference series is produced with geodetic data only, and consequently depends mostly on the IRIS intensive VLBI data for short period UT1 and LOD behavior. The prediction or “test” series uses the same geodetic data together with AAM analysis and AAM **forecast** data sets. In this series, however, all the data are not used. A series of filtering epochs are defined about which the data sets are decimated to simulate the quantity and frequency of data of each type that would normally be available for an operational filter run. Thus, no IRIS VLBI data are available within about 10 days of the filtering epoch, while AAM analysis data are available up to the time of filtering. Note that AAM forecast data are available beyond the filtering epoch, since they are forecasts that were made and **distributed** before the time of fil-

tering. The length of time between the last possible data point of a particular type and the filtering epoch is listed under “Typical Availability” in Table 1.

At the filter restart times shown in Figure 7, the full **Kalman** state vector and **covariance** matrix previously generated from a forward filter run using all preceding data are read from a disk file and used to restart the filtering process. Filtering continues forward in time with the subsequent, reduced set of data until the end of that filtering cycle, typically a 30-day time period. The backward filter then commences with the last measurement from the reduced data set, either geodetic or atmospheric, and continues backward in time until the start of that cycle. The two series are then vector weighted averaged to yield the prediction series for one cycle. The filter continues by reading in the state and **covariance** matrix for the next cycle. In the discussion that follows, all the prediction cycles are 30 days in length, with the filtering epoch occurring on day 20 of the cycle; hence, a 10 day UT 1 prediction is generated.

The prediction series for each cycle is difference with the reference series over the same time span, generating a time series of prediction errors for each cycle. One indicator of filtering accuracy is the RMS error at each day in the cycle, obtained by summing over all the cycles:

$$\epsilon_{\text{RMS}, i} = \left(\frac{1}{M} \sum_{j=1}^M \epsilon_{j,i}^2 \right)^{1/2} \quad (27)$$

where i is the day number in the cycle ($i = 1, \dots, N$, for cycles of N days), and j is the cycle number (with the test series consisting of M cycles). The difference between the test value and the truth value on day i of cycle j , $\epsilon_{j,i}$, is obtained by

$$\epsilon_{j,i} \equiv \mathbf{h}^T (\mathbf{x}_p - \mathbf{x}_r)_{j,i} \quad (28)$$

where \mathbf{x}_p and \mathbf{x}_r are the prediction and reference series state **vectors, respectively**, and \mathbf{h} is the vector that extracts that component or combination of components of interest from the difference vector (see, e.g., equation (19)). These RMS errors will be used to evaluate prediction accuracy in the studies presented below.

A number of caveats should be mentioned regarding the multiple case-study tool and the interpretation of the following figures. The case-study tool defines fixed epochs for running the filter to generate UT1 predictions, regardless of the data actually available at that epoch. In real operation, however, the operator may choose to run KEOF only when a new TEMPO measurement becomes available. In the case studies, for example, the last available TEMPO point usually lies between days 13 and 17 of the cycle, whereas in KEOF operation, a TEMPO point usually occurs on the equivalent of day 16 or 17 of the cycle. Thus, TEMPO data may play a more important role in actual filter operation than is suggested by the results shown below. Moreover, the data elimination strategy chosen (i.e., the “Typical Availability” of Table 1) assumes that the filter is run immediately after the weekly delivery of the non-TEMPO geodetic data types. In practice, geodetic data other than TEMPO may be several days older than assumed here (although recent, more timely, NAVNET data may be several days younger than assumed), **making** the actual importance of TEMPO and AAM data even greater than is suggested by this simulation study.

The role of atmospheric data

We have generated three case-study prediction time series, in which (1) only geodetic data were used to predict UT1, (2) AAM analysis data were used along with the geodetic data to predict UT1, and (3) both AAM analysis and 5-day forecast data were used to augment the geodetic data. The time series **consisted** of 4.5 years of data running from the beginning of 1987 to mid-1991, sufficient to form 55 cycles of 30 days length for the case study. Each series was difference with a reference UT 1 series created by filtering and smoothing the geodetic data only in the standard KEO Filter. These geodetic data sets had their biases, rates, and formal errors adjusted prior to filtering, as described in the previous section in regard to Figure 5.

**Fig. 8
near
here**

Figure 8 shows a one-year segment of these difference series. Although the **magni-**tude of the UT1 errors in Figure 8a vary with time, and no one series always possesses the smallest errors, it is clear that the geodetic-data-only series yields larger errors than the two

series incorporating atmospheric data. A similar conclusion may be drawn from the LOD error series of Figure 8b. Note that the LOD error series are noisier than the UT1 error series, a result of UT1 being the integral of LOD and integration being a smoothing operation.

**Fig. 9
near
here**

The RMS prediction errors for the three series are shown in Figure 9. The **geodetic-data-only** series errors begin to grow well before all the geodetic data are exhausted, diverging from the **geodetic-plus-AAM** curves more than five days before the filtering epoch in the case of UT 1 (Figure 9a), and even earlier for LOD (Figure 9b). Note that the growth in error when geodetic data only are filtered is consistent with the growth expected due to the stochastic excitation of the UT1 and LOD terms in the absence of data. By the time of the filtering epoch, the **geodetic-plus-AAM** series exhibits UT1 errors almost 0.5 ms smaller than those of the geodetic-data-only series. Given a DSN-required level of real-time UT1 accuracy of 0.6 ms, it appears that this goal can only be achieved if AAM data are employed. Including AAM forecast data does not produce significant benefit until three days after the filtering epoch, but it improves the UT1 estimate by up to 0.4 ms for a 10-day prediction.

The differences between the various curves are even more pronounced in the LOD component (Figure 9b), and the structures of the curves help to reveal the processes that influence the filtering. For example, errors in all the curves begin to grow as the high-precision IRIS and NAVNET **multibaseline** data drop out of the picture (day 6 in cycle). After the daily IRIS intensive data drop out (day 10 in cycle), the effect of daily AAM data can be seen. The geodetic-data-only curve continues to grow at a rate consistent with the **random-walk** model for LOD behavior, although it is somewhat constrained by the presence of TEMPO data. The curves incorporating AAM data show much smaller errors due to the constraints provided by the daily AAM. As the **geodetic-plus-AAM** analysis data curve loses its data (at day 19 in cycle), its error begins to grow at a rate similar to that of the **geodetic-data-only** error curve. Including AAM forecast data appears to significantly improve the prediction of LOD from the filtering epoch onwards,

This improvement in UT1 and LOD prediction due to the addition of AAM data to the current mix of geodetic data types appears to be robust. Similar results are seen with different time spans of data and different cycle lengths. The actual magnitudes of the RMS prediction errors can vary significantly depending on the time period considered, but the relative improvement provided by including AAM data remains substantial.

Fig. 10
near
here

Figure 9 presented the prediction error aggregated over many cycles. For any individual cycle, this error may be significantly larger or smaller. This is illustrated in Figure 10, where the UT 1 prediction errors at the filtering epoch (day zero) and at five days after the filtering epoch are shown for each cycle, for both geodetic data only and geodetic plus AAM and AAMF data. For day zero, errors are usually under 1 ms if AAM data are employed, but often exceed 2 ms without AAM. For day five, these numbers increase by a factor of two. Note, however, that even for predictions for day five made using geodetic data only, many cycles show errors of 0.5 ms or less. There is a hint of a seasonal effect on the errors, with larger negative errors seen around July and, when AAM data are included, around January also. Positive peaks tend to occur in October and April. This **seasonality** may be related to the variability of LOD, which tends to have millisecond-level jumps preferentially occurring at certain times of the year (see, *e.g.*, Figure 1).

The role of geodetic data

Fig. 11
near
here

We also investigated the quality of UT1 and LOD predictions when particular geodetic data sets were absent, but with atmospheric data included. The most influential geodetic data types for UT1 prediction (in an operational mode) are the TEMPO VLBI and the IRIS intensive data sets, as they provide the most timely information about the UT 1 component of Earth orientation. In Figure 11, these two data sets have alternately been deleted. Clearly, removing TEMPO data harms the estimate and prediction of UT1 and LOD after the IRIS intensive data become unavailable (day 10), whereas deleting IRIS intensive data only affects the higher-precision estimates generated prior to day 10 when all data types are still avail-

able. This plot illustrates well the need for a rapid-turnaround geodetic technique such as TEMPO in real-time UT1 estimation, even when atmospheric data are used.

**Fig. 12
near
here**

The benefits of more rapidly available geodetic data for both UT1 and LOD prediction are illustrated in Figure 12. The shortest turnaround times that the various techniques sometimes achieve are shown in the rightmost column of Table 1, next to the typical turnaround times for each data series. The prediction errors obtained with these rapidly available geodetic data and those resulting from typical data turnaround times are shown in the figure. Rapid geodetic data turnaround makes a substantial difference in UT1 and LOD prediction accuracy when atmospheric data are absent. With AAM analysis and forecast data, timely geodetic data again improve both the estimates and forecasts, but the level of improvement is smaller. Furthermore, from about day 20, the UT1 estimates made with standard turnaround geodetic data plus AAM analysis and forecast data are superior to those made with rapidly available geodetic data but without AAM. Hence, AAM data help to alleviate the urgency of obtaining the most timely geodetic data possible and the difficulties arising from occasional geodetic data outages.

A comment should be made regarding a phenomenon present in the LOD prediction error plots (Fig. 9b, 12b, and in particular, Fig. 11b) and, to a lesser extent, in the corresponding UT1 plots. This is a “ripple” effect in the prediction error curves, where errors of LOD (and UT1) appear to get worse, then improve, even after individual data types drop out. This rippling is a byproduct of both sparse data and correlations between state vector components, as well as, to some extent, the true variations in Earth rotation. To illustrate with a simple example, if UT1 measurements are only available every 5 days, errors in UT1 will be largest midway between the data points (as seen in the “no-IRIS intensive” curve of Fig. 11a prior to day 15). Similar behavior occurs for LOD, but since LOD is proportional to the time derivative of UT1, the errors reach their minima midway between UT1 points and their maxima at the times of the UT1 measurements (Fig. 11b).

These simulation studies demonstrate the benefits of employing AAM analysis and forecast data in predicting UT1 and LOD, even when the most timely geodetic data are available. Since AAM quantities are evaluated daily, they provide valuable information on the day-to-day variability of Earth rotation, especially important after the daily IRIS intensive data are no longer available. As geodetic data types drop out, the AAM data remain the only source of information on the longer period, larger amplitude LOD variations that have a substantial impact over five-to-ten days. These daily AAM measurements are thus a useful complement even to TEMPO, which are the timeliest geodetic data but are only available every three or four days and monitor UTO and variation of latitude rather than UT1 directly. Even if a daily geodetic measurement of UT1 were available in real time, such as that envisioned from the Global Positioning System (GPS) [Freedman, 1991; Lichten et al., 1992], AAM analysis and forecast data sets would still be useful as an independent estimate of the high-frequency behavior of LOD and as a predictor of its future behavior, respectively.

Formal uncertainties versus true errors

An important advantage of the **Kalman** filtering approach to data combination and prediction is the ability to provide formal uncertainties for the resulting estimates. It is desirable to assess the accuracy of these uncertainties by comparing them with actual errors. We have chosen to illustrate this comparison through the use of a quality factor, β , representing the square of the true error divided by the predicted variance as a function of day in the prediction cycle. The β value on day i in the cycle is thus defined to be

$$\beta = \frac{1}{M} \sum_{j=1}^M \frac{[\mathbf{h}(\mathbf{x}_p - \mathbf{x}_r)_{j,i}]^2}{\mathbf{h}(\mathbf{P}_p + \mathbf{P}_r)_{j,i} \mathbf{h}^T} \quad (29)$$

The numerator is the square of the desired component of the difference series (the $\epsilon_{j,i}$ defined in (28)) and the denominator is its approximate variance (approximate, because the prediction and reference covariance matrices are not independent).

Fig. 13
near
here

Figure 13 illustrates **these** β values for the three series shown in Figs. 8 and 9 for both UT1 and LOD components. Since nearly the same data are used in the prediction and reference smoothing early in a cycle, **the** β values for the first half of all the curves are small. As the geodetic data drop out (between days 5 and 17) the β values rise to levels reflecting the square of the ratio between prediction error and prediction uncertainty. Furthermore, early in each cycle, the predicted and reference formal uncertainties are similar in magnitude, while towards the end of the cycle the predicted variances will dominate in the denominator of (29).

The time period between day 15 and day 30 in the cycle (the last five days of smoothing and first 10 days of prediction) is most critical for near-real-time knowledge of Earth rotation, and this period exhibits the largest differences among the three curves shown. The geodetic-data-only case appears to be modeled best according to this test, as **its** β values never exceed -1.2, This implies a ratio of true error to predicted error of about 1.1. Although the geodetic-data-only prediction errors are substantially larger than those of the other two curves (see Fig. 9), the predicted uncertainties grow sufficiently fast to **hold** β close to one.

Alternatively, equation (29) can be looked at as a statistical measure of model accuracy. Assuming the predictions on corresponding days in different cycles to be independent and the statistical models presented above to be valid, (29) also represents a normalized chi-squared ($\tilde{\chi}^2$) estimate of model accuracy. With 55 cycles in the $\tilde{\chi}^2$ computation, the probability of seeing a $\tilde{\chi}^2$ value of 1.2 or greater is about 15%. Thus, the stochastic model for the behavior of UT1 and LOD within **KEOF** appears to accurately describe the true behavior of these quantities, yielding reliable uncertainty estimates.

When AAM analysis and/or forecast data are included, **the** β values are larger. The UT1 curve containing A AM forecast data reaches a maximum of about 2, denoting actual prediction errors about 1.4 times their formal uncertainties. The UT1 curves **peak near** the times of the last atmospheric data **point**; similarly, the AAM forecast curve for LOD has a

sharp peak at day 23 while the AAM analysis curve shows a more subdued peak at day 18, one day before the raw data cease for each curve. These peaks are evidence that the atmospheric data restrict the growth in the formal prediction uncertainty more effectively than the growth in the actual prediction error. The probability of obtaining a $\tilde{\chi}^2$ value this **large** is **vanishingly** small, implying that there is room for improvement in our modeling of the stochastic processes for AAM and AAMF.

Although prediction intervals longer than 10 days were not examined here, the trends of all the curves in Fig. 13 suggest that for periods beyond 10 days (i.e., as the effects of the AAM data fade), the β values remain between 1.0 and 1.5. Thus, they denote prediction errors no more than 2570 greater than their formal uncertainties.

These results suggest that the stochastic models and/or process noise levels of AAM and AAMF need to be modified if formal uncertainties accurate to better than a factor of 1.4 are desired for prediction times of several days. An improved model would either reduce the prediction errors or increase the formal uncertainties, the former option being preferred from the standpoint of prediction accuracy, of course. Currently, however, KEOF uncertainty estimates for larger prediction intervals (and predictions made without atmospheric data) are consistent with actual prediction errors.

KEOF versus the IERS Rapid Service

The JPL Kalman Earth Orientation Filter was designed to provide a real-time Earth orientation prediction capability as accurate as possible. The development of the TEMPO VLBI system and the implementation of AAM analysis and forecast data were intended to provide a superior UT1 short-term prediction capability. Other estimates and predictions of UT1 are available, however. The most timely of these are the predictions of UT1 provided by the IERS Rapid Service [McCarthy and Luzum, 1991; IERS, 1992a]. A comparison of the UT1 predictions distributed by the Rapid Service in IERS Bulletin A and the corresponding KEOF predictions is shown in Figure 14 for a six month period in 1992.

Fig. 14
near
here

Three curves are shown in which: a) the operational, twice-weekly KEOF predictions of UT1 are difference with the (after-the-fact) Bulletin A smoothing, b) weekly KEOF UT1 predictions are difference with the Bulletin A smoothing, and c) weekly Bulletin A predictions are difference with the Bulletin A smoothing. Operational KEOF predictions are usually made on Tuesdays and Fridays, while Bulletin A predictions are generated on Thursdays, immediately after the weekly deliveries of geodetic data from the various analysis centers. The weekly KEOF predictions made on the following Fridays employ the same geodetic data except for (usually) one additional TEMPO point plus AAM analysis and forecast data. The weekly KEOF runs on the subsequent Tuesdays include only one additional TEMPO point, together with daily AAM data.

As Fig. 14 shows, the KEOF predictions are usually more accurate than the IERS Bulletin A predictions both for the twice-weekly operational KEOF runs and for weekly KEOF predictions made with the same frequency and at nearly the same time as those of the Rapid Service. The RMS scatters of the KEOF predictions minus the Bulletin A reference smoothing (after removing mean differences) are 0.49 ms (twice-weekly) and 0.77 ms (weekly), while the RMS scatter for the Bulletin A predictions minus the Bulletin A smoothing is 1.26 ms. This superior performance is at least partially due to the inclusion of AAM and more timely TEMPO data in the KEOF solutions, and may also be a result of the different UT1 models and prediction strategies employed. It is also clear from Fig. 14 that twice weekly predictions provide substantial improvement over those made once per week. “

5. Concluding Remarks

We have shown that, for the purpose of near-real-time estimation and short-term prediction of UT1 and LOD variations, meteorologically-determined atmospheric angular momentum information is an important adjunct to geodetic measurements of Earth orientation. Both AAM analysis and 5-day forecast data have a significant impact on the ability to estimate and predict UT1 and LOD using the JPL **Kalman** Earth Orientation Filter, particu-

larly when dense geodetic data are lacking. The AAM analysis data are of greatest value from the time when daily geodetic estimates of UT1 cease through the epoch when the filter is run, while the AAM forecast data are of benefit from the filtering epoch onward. Where dense and high quality geodetic data are available, the AAM data with their currently assumed formal errors do not provide any statistically significant improvement, although they do provide an independent check on the overall high-frequency variability of LOD. Inclusion of AAM analysis and forecast data improve UT1 and LOD predictions even though there is evidence that the stochastic AAM and AAMF models currently used in KEOF may not be optimal. Improvements in these models are currently being studied and should soon lead to even better UT1 and LOD predictions.

TEMPO VLBI data are a critical geodetic data set for near-real-time knowledge of UT1 due to their rapid turnaround time. Future rapid-turnaround geodetic measurements of UT1, perhaps from GPS, may improve our prediction capabilities even further. Even with rapid-turnaround geodetic data, however, AAM data will be of benefit for UT1 and LOD prediction.

Ongoing research in a number of areas may lead to improvements in our filtering capabilities. Most of our present knowledge of UT1 and LOD behavior at periods of a few days is derived from studies of the IRIS intensive VLBI data. The errors in these data can best be ascertained by comparison with independent observations, few of which exist, however. In addition, sub-daily variations in UT1 may alias into the IRIS intensive series due to the one-hour measurement time span and near-daily spacing of the data. Comparisons are now being performed with independent VLBI and GPS data [Herring and Dong, 1991; Lichten et al., 1992]. High-frequency variations in UT1 due to diurnal and semidiurnal ocean tides are being incorporated into the preprocessing and study of the IRIS data and into an R&D version of the filter [Gross, 1992]. These investigations should yield improved knowledge of the true behavior of the Earth's rotation at periods shorter than about 10 days.

The AAM data sets are also subject to a variety of errors, Improvements in the physical and numerical models of the global meteorological forecasting software are constantly occurring, sometimes having profound effects on the resulting AAM estimates and forecasts. There are known deficiencies in the temporal and spatial distribution of the raw meteorological data used in operational weather forecasting, Some of these may be alleviated in the coming years by new satellite remote sensing tools. For example, our knowledge of winds in the southern hemisphere and high in the atmosphere should soon be improved by instruments in orbit. There are also a number of unresolved issues dealing with the use and reliability of currently available estimates of stratospheric AAM and the AAM pressure terms; these are presently under investigation [Freedman and Dickey, 1991, for example].

The filtering scheme incorporated within KEOF must reflect the changing character of the raw data sets used. To this end, studies are regularly being performed to assess the corrections, such as biases, rates, and error scaling, that may need to be applied to the raw data. In addition, we are currently reevaluating the stochastic models for the various UTPM components, using the most recent data sets. Finally, as atmospheric data are becoming available in near-real time from other meteorological centers, it may be beneficial to switch to a different AAM series or combination of series better suited as a proxy LOD data set.

Appendix A

This appendix contains the explicit derivation of some of the more complicated matrices used in forward filtering. Appendix B contains similar quantities for the backward filter. Only the **final** five elements of the vectors and final 5x5 elements of the matrices will be **presented** here, as the first six elements which are associated with polar motion have been described elsewhere [Morabito et al., 1988; Gross et al., manuscript in preparation]. From equations (5-7), (9), and (11), equation (4) can be expanded to

$$\frac{d\mathbf{x}}{dt} = \begin{bmatrix} \dot{U} \\ \dot{L} \\ \dot{\mu}_A \\ \dot{b} \\ \dot{\mu}_F \end{bmatrix} = \mathbf{F}\mathbf{x} + \boldsymbol{\omega} = \begin{bmatrix} 0 & -1 & 0 & 0 & 0 \\ 0 & 0 & 0 & 0 & 0 \\ 0 & 0 & 0 & 0 & 0 \\ 0 & 0 & 0 & 0 & 0 \\ 0 & 0 & 0 & 0 & -\tau_i^{-1} \end{bmatrix} \begin{bmatrix} U \\ L \\ \mu_A \\ b \\ \mu_F \end{bmatrix} + \begin{bmatrix} 0 \\ \omega_L \\ \omega_A \\ 0 \\ \omega_F \end{bmatrix} \quad (\text{A1})$$

Using the F matrix given above, the transition matrix@ can be derived using (13)

$$\Phi(\Delta t) = \exp(\mathbf{F} \Delta t) = \sum_{k=0}^{\infty} \frac{\mathbf{F}^k \Delta t^k}{k!} = \begin{pmatrix} 1 & -\Delta t & 0 & 0 & 0 \\ 0 & 1 & 0 & 0 & 0 \\ 0 & 0 & 1 & 0 & 0 \\ 0 & 0 & 0 & 1 & 0 \\ 0 & 0 & 0 & 0 & \exp\left(\frac{-\Delta t}{\tau_i}\right) \end{pmatrix} \quad (\text{A2})$$

where $\Delta t = t_i - t_{i-1}$. This matrix multiplied by the state vector estimate according to (14) yields the propagated state components listed in (16).

The propagated state error **covariance** matrix (15) can be broken into two parts: the previous covariance matrix propagated forward in time, and the added excitation due to the process noise models. If the previous covariance matrix were diagonal (usually only true of the a priori **covariance** matrix), propagation would yield

$$\begin{aligned} \Phi(\Delta t) \hat{\mathbf{P}}_{i-1} \Phi^T(\Delta t) &= \Phi(\Delta t) \begin{bmatrix} \sigma_U^2 & 0 & 0 & 0 & 0 \\ 0 & \sigma_L^2 & 0 & 0 & 0 \\ 0 & 0 & \sigma_{\mu_A}^2 & 0 & 0 \\ 0 & 0 & 0 & \sigma_b^2 & 0 \\ 0 & 0 & 0 & 0 & \sigma_{\mu_F}^2 \end{bmatrix} \Phi^T(\Delta t) \\ &= \begin{bmatrix} \sigma_U^2 + \Delta t^2 \sigma_L^2 & -\Delta t \sigma_L^2 & 0 & 0 & 0 \\ -\Delta t \sigma_L^2 & \sigma_L^2 & 0 & 0 & 0 \\ 0 & 0 & \sigma_{\mu_A}^2 & 0 & 0 \\ 0 & 0 & 0 & \sigma_b^2 & 0 \\ 0 & 0 & 0 & 0 & \sigma_{\mu_F}^2 \exp\left(\frac{-2\Delta t}{\tau_i}\right) \end{bmatrix} \end{aligned} \quad (\text{A3})$$

Only the uncertainties in UT1 and the AAM forecast (μ_F) change with time. This pattern of time dependence remains even for a full **covariance** matrix; thus, only the U and μ_F variances and covariances of a propagated state **covariance** matrix are functions of time.

The stochastic model adds noise to the system according to

$$\begin{aligned}
 & \int_{t_{i-1}}^{t_i} \Phi(t_i - \eta) Q \Phi^T(t_i - \eta) d\eta \\
 &= \int_{t_{i-1}}^{t_i} \begin{pmatrix} Q_L(t_i - \eta)^2 & -Q_L(t_i - \eta) & 0 & 0 & 0 \\ -Q_L(t_i - \eta) & Q_L & 0 & 0 & 0 \\ 0 & 0 & Q_A & 0 & 0 \\ 0 & 0 & 0 & 0 & 0 \\ 0 & 0 & 0 & 0 & Q_F \exp\left(\frac{-2(t_i - \eta)}{\tau_i}\right) \end{pmatrix} d\eta \\
 &= \begin{pmatrix} \frac{Q_L}{3} \Delta t^3 & -\frac{Q_L}{2} \Delta t^2 & 0 & 0 & 0 \\ -\frac{Q_L}{2} \Delta t^2 & Q_L \Delta t & 0 & 0 & 0 \\ 0 & 0 & Q_A \Delta t & 0 & 0 \\ 0 & 0 & 0 & 0 & 0 \\ 0 & 0 & 0 & 0 & \frac{Q_F \tau_i}{2} \left[1 - \exp\left(\frac{-2 \Delta t}{\tau_i}\right)\right] \end{pmatrix} \quad (A4)
 \end{aligned}$$

All the uncertainties except that for the b term are functions of time. The only off-diagonal terms produced are the cross-correlations between UT1 and LOD. When the operational KEOF values for Q_i from Table 3 are inserted in (A4), the error sigmas shown in (23) are produced.

Appendix B

This appendix discusses the main differences between forward filtering and backward filtering. The system model for a backward Kalman filter maybe derived from the forward model (equation 4) by defining a new time variable ζ , where [Gelb, 1974]

$$\zeta \equiv T - t \quad (B1)$$

In forward filtering t goes from 0 to T , while in backward filtering t goes from T to 0. Therefore, the new variable ζ runs from 0 to T in backward filtering, just as t does in forward filtering. The new system model is

$$\frac{d\mathbf{x}(\zeta)}{d\zeta} = \frac{d\mathbf{x}(\zeta)}{dt} \frac{dt}{d\zeta} = -\frac{d\mathbf{x}(\zeta)}{dt} - F\mathbf{x}(\zeta) - \omega(\zeta) \equiv F'\mathbf{x}(\zeta) + \omega'(\zeta) \quad (\text{B2})$$

The final form of (B2) is identical to (4), with F replaced by F' and ω replaced by $(J.)'$. Thus equations (14) and (15) become in backward filtering

$$\hat{\mathbf{x}}_i = \Phi'(\zeta_i - \zeta_{i-1}) \hat{\mathbf{x}}_{i-1} \quad (\text{B3})$$

and

$$\hat{\mathbf{P}}_i = \Phi'(\zeta_i - \zeta_{i-1}) \hat{\mathbf{P}}_{i-1} \Phi'^T(\zeta_i - \zeta_{i-1}) + \int_{\zeta_{i-1}}^{\zeta_i} \Phi'(\zeta_i - \lambda) Q \Phi'^T(\zeta_i - \lambda) d\lambda \quad (\text{B4})$$

where $\zeta_{i-1} < \zeta_i$. Note that $Q' = Q$, because the power spectral density of $-\omega(\zeta)$ is the same as the power spectral density of $\omega(t)$.

In parallel with equations (A2), (A3), and (A4), the backward filter yields

$$\Phi'(\Delta\zeta) = \exp(F' \Delta\zeta) = \exp(F(-\Delta\zeta)) = \begin{vmatrix} 1 & \Delta\zeta & 0 & 0 & 0 \\ 0 & 1 & 0 & 0 & 0 \\ 0 & 0 & 1 & 0 & 0 \\ 0 & 0 & 0 & 1 & 0 \\ 0 & 0 & 0 & 0 & \exp\left(\frac{\Delta\zeta}{\tau_i}\right) \end{vmatrix} \quad (\text{B5})$$

$$\Phi'(\Delta\zeta) \hat{\mathbf{P}}_{i-1} \Phi'^T(\Delta\zeta) = \begin{vmatrix} \sigma_u^2 + \Delta\zeta^2 \sigma_L^2 & \Delta\zeta \sigma_L^2 & 0 & 0 & 0 \\ \Delta\zeta \sigma_L^2 & \sigma_L^2 & 0 & 0 & 0 \\ 0 & 0 & \sigma_{\mu_a}^2 & 0 & 0 \\ 0 & 0 & 0 & \sigma_b^2 & 0 \\ 0 & 0 & 0 & 0 & \sigma_{\mu_r}^2 \exp\left(\frac{2\Delta\zeta}{\tau_i}\right) \end{vmatrix} \quad (\text{B6})$$

$$\begin{aligned}
& \int_{\zeta_{i-1}}^{\zeta_i} \Phi'(\zeta_i - \lambda) \mathbf{Q} \Phi'^T(\zeta_i - \lambda) d\lambda \\
&= \int_{\zeta_{i-1}}^{\zeta_i} \begin{pmatrix} Q_L(\zeta_i - \lambda)^2 & Q_L(\zeta_i - \lambda) & 0 & 0 & 0 \\ Q_L(\zeta_i - \lambda) & Q_L & 0 & 0 & 0 \\ 0 & 0 & Q_A & 0 & 0 \\ 0 & 0 & 0 & 0 & 0 \\ 0 & 0 & 0 & 0 & Q_F \exp\left[\frac{2(\zeta_i - \lambda)}{\tau_i}\right] \end{pmatrix} d\lambda \\
&= \begin{pmatrix} \frac{Q_L}{3} \Delta \zeta^3 & \frac{Q_L}{2} \Delta \zeta^2 & 0 & 0 & 0 \\ \frac{Q_L}{2} \Delta \zeta^2 & Q_L \Delta \zeta & 0 & 0 & 0 \\ 0 & 0 & Q_A \Delta \zeta & 0 & 0 \\ 0 & 0 & 0 & 0 & 0 \\ 0 & 0 & 0 & 0 & \frac{Q_F \tau_i}{2} \left[\exp\left(\frac{2\Delta \zeta}{\tau_i}\right) - 1 \right] \end{pmatrix} \quad (B7)
\end{aligned}$$

Equations (B5) and (B6) could be obtained directly from (A2) and (A3) by changing the sign of the time arguments, but equation (B7) must be derived by integration. Although most of the state element uncertainties have the same form both forwards and backwards, the backward filter yields qualitatively different behaviors for the μ_F estimate, its propagated error (B6) and its excitation (B7).

Acknowledgments

We wish to thank K. Deutsch and S. G. Mulligan who implemented a major portion of the computer code for the operational version of KEOF, S. H. Oliveau for the routine operation of KEOF, and R. S. Gross for many useful discussions and critical reviews of this manuscript. The work described in this paper was carried out by the Jet Propulsion Laboratory, California Institute of Technology, under contract with the National Aeronautics and Space Administration.

References

- Barnes, R. T. H., R. Hide, A. A. White, and C. A. Wilson, "Atmospheric Angular Momentum Fluctuations, Length-of-Day Changes and Polar Motion," *Proc. R. Soc. London, Ser. A*, 387,31-73, 1983.
- Bell, M. J., R. Hide, and G. Sakellariades, "Atmospheric Angular Momentum Forecasts as Novel Tests of Global Numerical Weather Prediction Models," *Phil. Trans. Roy. Soc. Lond. A*, 334,55-92, 1991.
- Dickey, J. O., S. L. Marcus, J. A. Steppe, and R. Hide, "An investigation of the Earth's angular momentum budget at high frequencies (abstract)," *EOS Trans. Am. Geophys. Un.*, 70, 1055, 1989.
- Dickey, J. O., S. L. Marcus, J. A. Steppe, and R. Hide, "The Earth's Angular Momentum Budget on Subseasonal Time Scales," *Science*, 255,321-324, 1992.
- Eanes, R. J., and M. M. Watkins, "Earth orientation and site coordinates from the Center for Space Research solution," in *IERS Technical Note 11: Earth orientation, reference frames and atmospheric excitation functions submitted for the 1991 IERS Annual Report*, P. Chariot (ed.), pp. 75-79, International Earth Rotation Service, Central Bureau of IERS-Observatoire de Paris, 1992.
- Eubanks, T. M., J. A. Steppe, and J. O. Dickey, "Filtering and Prediction of Earth Rotation Variations Using Atmospheric Angular Momentum Data (abstract)," *EOS, Trans. AGU*, 68, 1244, 1987.
- Eubanks, T. M., J. A. Steppe, J. O. Dickey, and P. S. Callahan, "A spectral analysis of the Earth's angular momentum budget," *J. Geophys. Res.* **90**, 5385-5404, 1985.
- Freedman, A. P., "Measuring Earth Cementation With the Global Positioning System," *Bulletin Géodésique*, 65,53-65, 1991.
- Freedman, A. P., and J. O. Dickey, "Intercomparison of AAM Analysis and Forecast Data in UT 1 Estimation and Prediction" in *Proceedings of the AGU Chapman Conference on Geodetic VLBI: Monitoring Global Change* (Washington DC, April 22-26, 1991),

pp. 279-293, NOAA Technical Report NOS 137 NGS 49, NOS/NOAA, Rockville, MD, 1991.

Gelb, A. (Ed), *Applied Optimal Estimation*, 374 pp., The M.I.T. Press, Cambridge, MA, 1974.

Gross, R. S., "A combination of Earth orientation data: **SPACE91**," in *IERS Technical Note 11: Earth orientation, reference frames and atmospheric excitation functions submitted for the 1991 IERS Annual Report*, P. Chariot (cd.), pp. 113-118, International Earth Rotation Service, Central Bureau of IERS-Observatoire de Paris, 1992,

Gross, R. S., and T. M. Eubanks, "Estimating the "Noise" Component of Various Atmospheric Angular Momentum Time Series (abstract)," *EOS, Trans. AGU*, 69, 1153, 1988.

Gross, R. S., T. M. Eubanks, J. A. Steppe, A. P. Freedman, J. O. Dickey, and T. F. Runge, "A Kalman Filter-Based Approach to Combining Space-Geodetic Earth Orientation Series," *J. Geophys. Res.*, (to be submitted), 1993.

Gross, R. S., J. A. Steppe, and J. O. Dickey, "The Running RMS Difference Between Length-of-Day and Various Measures of Atmospheric Angular Momentum," in *Proceedings of the AGU Chapman Conference on Geodetic VLBI: Monitoring Global Change* (Washington DC, April 22-26, 1991), pp. 238-258, NOAA Technical Report NOS 137 NGS 49, NOS/NOAA, Rockville, MD, 1991.

Herring, T. A., and D. Dong, "Current and Future Accuracy of Earth Rotation Measurements," in *Proceedings of the AGU Chapman Conference on Geodetic VLBI: Monitoring Global Change* (Washington DC, April 22-26, 1991), pp. 306-324, NOAA Technical Report NOS 137 NGS 49, NOS/NOAA, Rockville, MD, 1991.

Hide, R., N. T. Birch, L. V. Morrison, D. J. Shea, and A. A. White, "Atmospheric angular momentum fluctuations and changes in the length of the day," *Nature*, 286, 114-117, 1980.

Hide, R., and J. O. Dickey, "Earth's Variable Rotation," *Science*, 253, 629-637, 1991.

IERS, *1991 IERS Annual Report*, International Earth Rotation Service, Central Bureau of the IERS-Observatoire de Paris, July, 1992a.

IERS, *IERS Technical Note 11: Earth orientation, reference frames and atmospheric excitation functions submitted for the 1991 IERS Annual Report*, P. Chariot (cd.), International Earth Rotation Service, Central Bureau of the IERS-Observatoire de Paris, June, 1992b.

JPL, "Preliminary Support Instrumentation Requirements Document(SIRD)," Cassini Flight Project, Jet Propulsion Laboratory, Doe. 699-501, August, 1991.

King, N. E., *Multiple Taper Spectral Analysis of Earth Rotation Data*, Ph.D. Thesis, 202 pp., University of California, San Diego(UCSD), 1990.

Lambeck, K., *The Earth's Variable Rotation: Geophysical Causes and Consequences*. 449 pp., Cambridge University Press, Cambridge, 1980.

Lambeck, K., *Geophysical Geodesy*. 718 pp., Oxford University Press, Oxford, 1988.

Lichten, S. M., S. L. Marcus, and J. O. Dickey, "Sub-Daily Resolution of Earth Rotation Variations With Global Positioning System Measurements," *Geophys. Res. Lett.*, **19**, 537-540, 1992.

McCarthy, D. D., and B. J. Luzum, "Prediction of Earth orientation," *Bulletin Géodésique*, **65**, 18-21, 1991.

Morabito, D. D., T. M. Eubanks, and J. A. Steppe, "Kalman Filtering of Earth Orientation Changes," in *The Earth's Rotation and Reference Frames for Geodesy and Geodynamics* (Proceedings of the 128th Symposium of the International Astronomical Union, Coolfont, West Virginia, 20-24 October, 1986), pp. 257-267, Kluwer Acad. Publ., Dordrecht, Holland, 1988.

Morgan, P. J., R. W. King, and I. I. Shapiro, "Length of Day and Atmospheric Angular Momentum: A Comparison for 1981 -1983," *J. Geophys. Res.*, **90**, 12645-12652, 1985.

- Rosen, R. D., and D. A. Salstein, "Variations in Atmospheric Angular Momentum on Global and Regional Scales and the Length of Day," *J. Geophys. Res.*, 88, 5451-5470, 1983.
- Rosen, R. D., and D. A. Salstein, "Contribution of Stratospheric Winds to Annual and Semi-annual Fluctuations in Atmospheric Angular Momentum and the Length of Day," *J. Geophys. Res.*, 90, 8033-8041, 1985.
- Rosen, R. D., D. A. Salstein, A. J. Miller, and K. Arpe, "Accuracy of Atmospheric Angular Momentum Estimates from Operational Analyses," *Mon. Wea. Rev.*, 115, 1627-1639, 1987a.
- Rosen, R. D., D. A. Salstein, T. Nehrkorn, M. R. P. McCalla, A. J. Miller, J. O. Dickey, T. M. Eubanks, and J. A. Steppe, "Medium Range Numerical Forecasts of Atmospheric Angular Momentum," *Mon. Wea. Rev.*, 115, 2170-2175, 1987b.
- Rosen, R. D., D. A. Salstein, and T. Nehrkorn, "Predictions of Zonal Wind and Angular Momentum by the NMC Medium-Range Forecast Model During 1985 -89," *Mon. Wea. Rev.*, 119, 208-217, 1991.
- Rosen, R. D., D. A. Salstein, and T. M. Wood, "Discrepancies in the Earth-Atmosphere Angular Momentum Budget," *J. Geophys. Res.*, 95, 265-279, 1990.
- Runge, T. F., "UTPM Calibration Accuracy for Magellan," internal document, Jet Propulsion Laboratory, IOM 335.5-87.81, April, 1987.
- Steppe, J. A., R. S. Gross, O. J. Severs, and S. H. Oliveau, "Smoothed, standard-coordinate Earth rotation from Deep Space Network VLBI: 1992," in *IERS Technical Note 11: Earth orientation, reference frames and atmospheric excitation functions submitted for the 1991 IERS Annual Report*, P. Chariot (cd.), pp. 27-28, International Earth Rotation Service, Central Bureau of IERS-Observatoire de Paris, 1992a.
- Steppe, J. A., S. H. Oliveau, and O. J. Severs, "Earth rotation parameters from DSN VLBI: 1992," in *IERS Technical Note 11: Earth orientation, reference frames and atmospheric excitation functions submitted for the 1991 IERS Annual Report*, P. Chariot (cd.), pp. 17-26, International Earth Rotation Service, Central Bureau of IERS-Observatoire de Paris, 1992b.

- Sung, L.-Y., "Maximum Likelihood Estimation of Biases, Rates, Scaling Factors and Additive **Covariance** Matrix for Earth Orientation Data Series (abstract)," *EOS, Trans. A, G. U.*, 73 (14), Spring Meeting **Suppl.**, 80, 1992.
- Treuhaft, R., and L. Wood, "Revisions in the Differential VLBI Error Budget and Applications for Navigation in Future Missions," internal document, Jet Propulsion Laboratory, **IOM 335.4-601**, December, 1986,
- Yoder, C. F., J. G. Williams, and **M. E. Parke**, "Tidal Variations of Earth Rotation," *J. Geophys. Res.*, **86**,881-891, 1981.

Table 1. Operational **KEOF** Data Sets

Name	Type	Reported Quantities	Frequency	Availability	
				Typical	Rapid
TEMPO	VLBI	UT0/Var. Lat. ^b	twice/week ^c	2-3 days	1 day
IRIS multibaseline	VLBI	PM, UT1	weekly ^d	14 days	10 days
IRIS intensive	VLBI	UT1	daily	10 days	7 days
NAVNET	VLBI	PM, UT1	weekly ^e	14 days ^f	10 days
CSR (U. Texas)	SLR	PM, UT1 ^g	once/3-days	5 days	3 days
JPL	LLR	UT0/Var. Lat. ^b	irregular	long	1 day
NMC O-hour	AAM	AAM analysis	daily	1-2 day	1 day
NMC 5-day	AAMF	AAM forecasts	daily		

^a All techniques experience data dropouts, so are not strictly regular.

^b **UT0** and **Variation-of-Latitude** are linear combinations of **polar** motion and **UT1**.

^c TEMPO data are acquired on two baselines, each of which is measured once per week.

^d Prior to April 1991, IRIS multibaseline data were obtained every five days.

^e NAVNET data are staggered in time with IRIS multibaseline data beginning in 1991.

^f The most recent NAVNET data are available more rapidly, with a 6 to 10 day delay.

^g CSR UT1 data are not currently employed by KEOF (see text).

Note: IRIS, NAVNET, and CSR data are only distributed once per week, and may thus be up to one week older than shown in the availability column.

Table 2. State Vector and Covariance Matrix Parameter Definitions

Parameter	Definition
x	Polar motion X
y	Polar motion Y
μ_1	Polar motion excitation ($\equiv \chi_1$) ^{a, b}
μ_2	Polar motion excitation minus annual wobble excitation ($\equiv \chi_2 - S$) ^{a, b}
s	Annual wobble excitation ^b
\dot{S}	Time derivative of S ^b
u	UT1-TAI ^c
L	Excess length of day, normalized ^{c, d}
μ_A	Difference between AAM and LOD (AAM - LOD) ^d
b	Bias between AAM analyses and forecasts ($AAMF - AAM - \mu_F$) ^d
μ_F	Difference between AAM forecasts and analyses, with a bias term removed ($AAMF - AAM - b$) ^d
ω_i	White noise stochastic excitation for corresponding term i
τ_i	AAM forecast model time constant

^a Formulation of Barnes et al, [1983].

^b See Morabito et al. [1988].

^c All tides from 5 days to 18.6 years removed according to Yoder et al. [1981].

^d Parameters L , μ_A , b , and μ_F represent LOD and AAM quantities normalized by Λ_0 , e.g., $L \equiv \Delta/\Lambda_0$.

Table 3. Stochastic Model Parameter Values

Model Parameter	Value
Q_L	0.0036 ms ² /day ³
Q_A	0.0004 ms ² /day ³
Q_F	0.00225 ms ² /day ³
τ_i	5 days

The Q values are two-sided power spectral densities, i.e., they represent the PSD when power is distributed over both positive and negative frequencies. See Eubanks et al. [1985; 1987]. Units of Q are ms²/day³ when LOD and AAM are normalized by Λ_0 , ms²/day without normalization.

Figure Captions

Fig. 1. Comparison between length of day (LOD) and atmospheric angular momentum (AAM), (a) Time series comparison over two years. (b) Squared coherence (after Dickey et al. [1992]; the **95%** confidence level for an 11-point smoothing is shown).

Fig. 2. Power spectral density (PSD) of LOD, AAM (both analyses and forecasts), and their differences. (a) LOD and AAM, (b) AAM analyses and 5-day forecasts, The random-walk stochastic model for LOD and the autoregressive (AR 1) model for the difference of AAMF and AAM are also shown, The confidence interval on the spectral estimates and the spectral smoothing are indicated. (Power spectra are one-sided, i.e., they contain the total power of the time series but extend over positive frequencies only.)

Fig. 3. Set of synthetic input data for KEOF response test. (a) Input UT1 data, with defining function and one-sigma formal error, (b) Input AAM and AAMF data sets, with defining functions and one-sigma error.

Fig. 4. Smoothed KEOF output after receiving input data sets shown in Fig. 3. (a) Output UT1 series, (b) output UT1 formal error (log scale), (c) output LOD, AAM, and AAMF series, (d) output LOD, AAM, and AAMF one-sigma formal errors (log scale).

Fig. 5. Differences between input measurement (raw) data and smoothed KEOF output series for a sample KEOF filter run using a full set of geodetic and atmospheric data. Also shown are the formal errors of both the input data (dashed line) and output data (solid line). Only the UT1 component is shown, and only for those data types that directly report UT1 (IRIS multibaseline, IRIS intensive, NAVNET). RMS scatter of the residuals is also shown.

Fig. 6. Differences in KEOF output when atmospheric data are either included or not included in a full multi-year smoothing, compared to the formal error of the smoothed series

with AAM included. (a) UT1 component. (b) LOD component. RMS scatters of the differences are shown,

Fig. 7, Schematic view of multiple case-study filtering. See text for explanation.

Fig. 8. One year set of prediction errors emerging from the filter case-study for three raw data sets: geodetic data only, geodetic plus AAM analysis data, and geodetic plus AAM analysis and 5-day forecast data. (a) UT1 component. (b) LOD component.

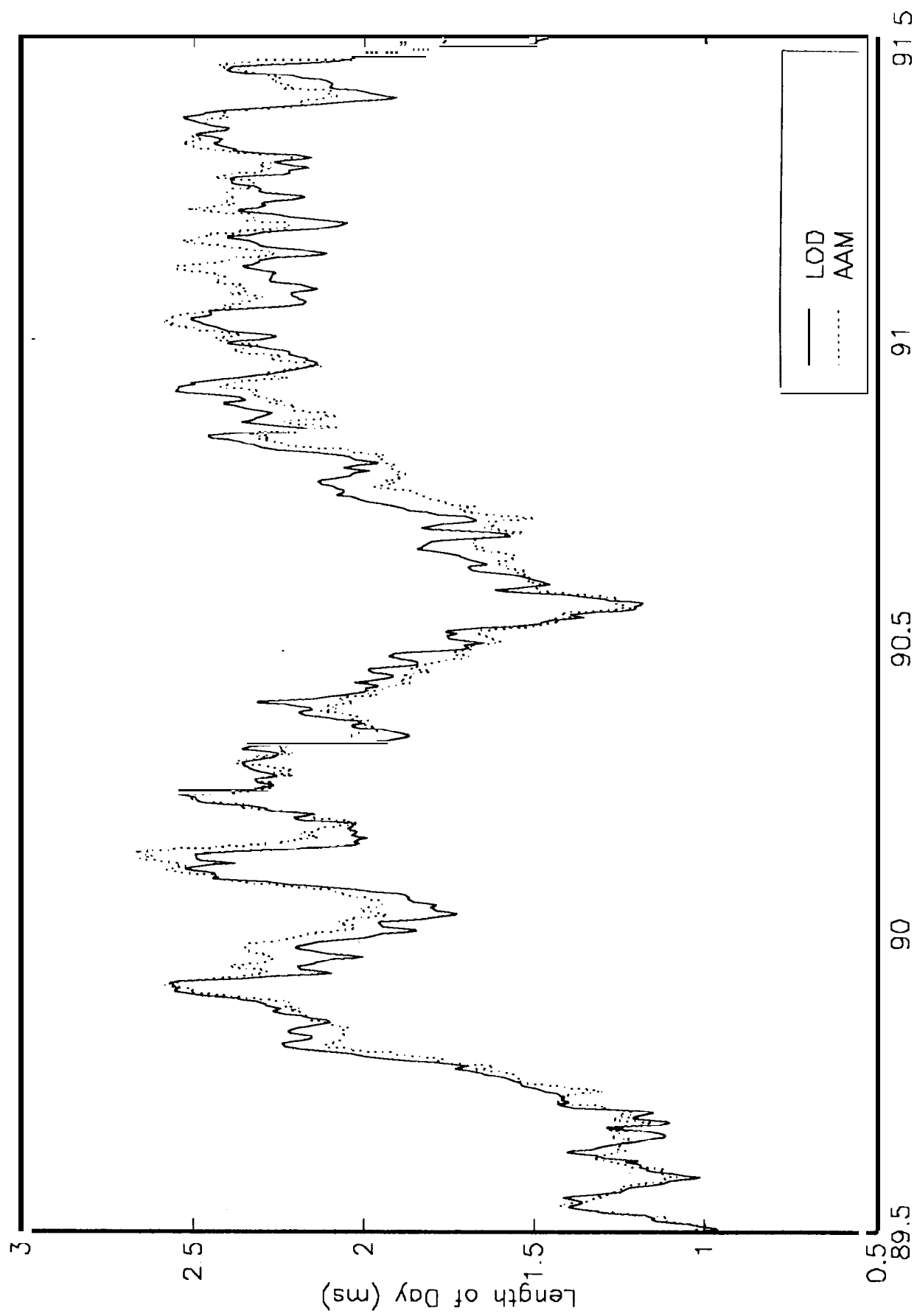
Fig. 9. RMS prediction errors over 55 thirty-day cycles spanning 4.5 years for the three data sets shown in Fig. 8. (a) UT 1 prediction errors. (b) LOD prediction errors, with the time intervals within which the various raw data may fall also shown. The one-sigma error uncertainties predicted from the stochastic excitation component of the filter model (assuming the state to be known perfectly on day 10 of the cycle) are also shown.

Fig. 10. UT1 prediction errors in every cycle from the case study for geodetic data sets both with and without the AAM. (a) Prediction errors at the filtering epoch (day zero of prediction). (b) Prediction errors on day five.

Fig. 11. RMS prediction errors made with TEMPO data absent, IRIS intensive data absent, and all data present. Atmospheric data are included in all three filter runs. (a) UT1 component, (b) LOD component. The TEMPO and IRIS intensive data windows are shown. Note the change in scale from Fig. 9.

Fig. 12. RMS prediction errors made assuming either standard data turnaround times or rapidly available data, both with and without AAM data. (a) UT1 component. (b) LOD component.

Fig. 13. Quality factor β curves (see text) for the three data sets shown in Figs. 8 and 9. (a) UT1 component. (b) LOD component. Interpreting β as a **chi-squared** quantity and



Time in years since 1800

Figure 1a.

assuming valid statistical models, the region within which there is a 99% probability of the β value falling is shown,

Fig. 14. Comparison of UT1 predictions over a six-month period. (a) Twice-weekly (operational) KEOF predictions minus Bulletin A smoothing. (b) Weekly KEOF predictions minus Bulletin A smoothing. (c) Weekly Bulletin A predictions minus Bulletin A smoothing. The mean and standard deviation for each difference series are shown,

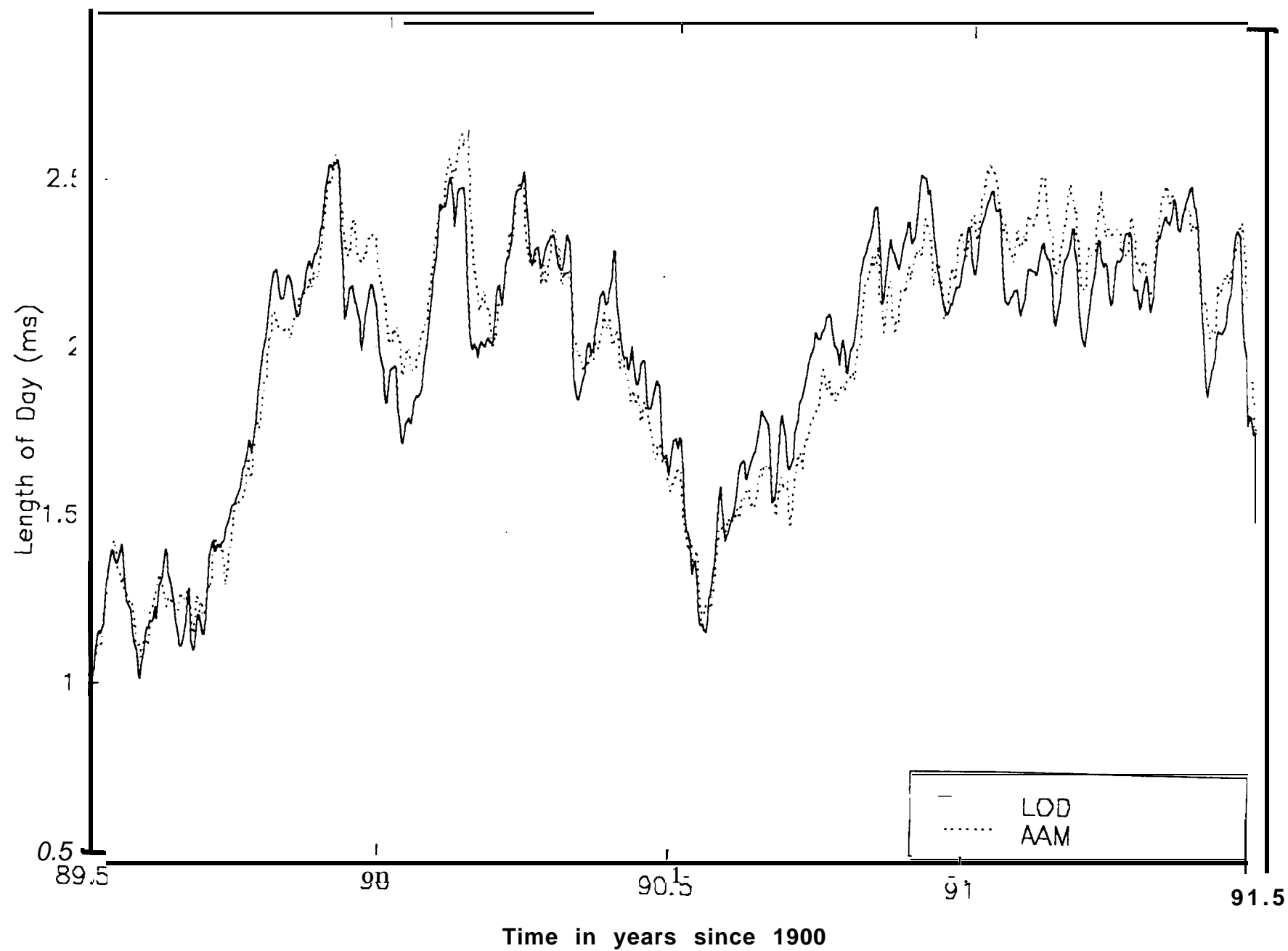


Figure 1a

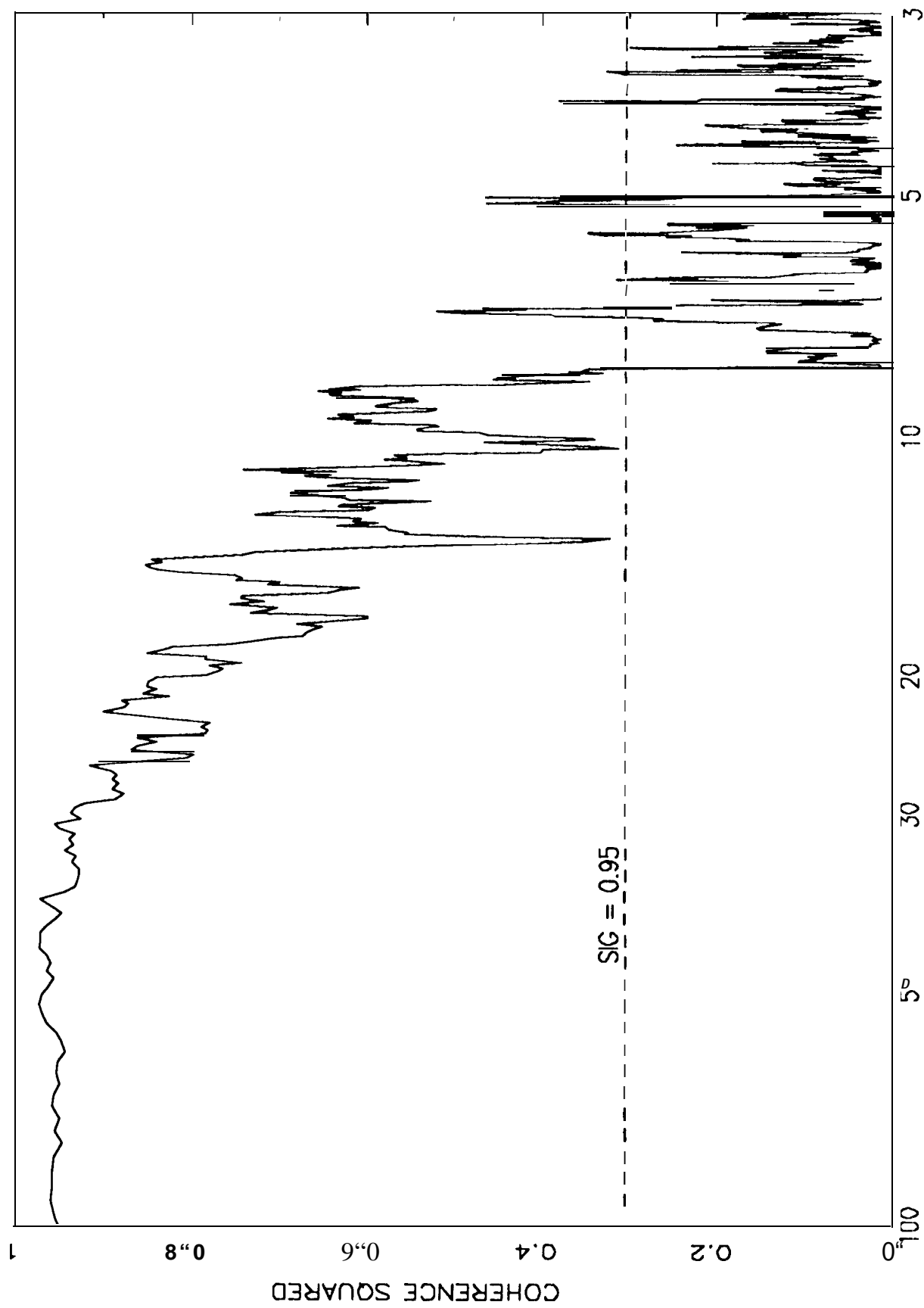
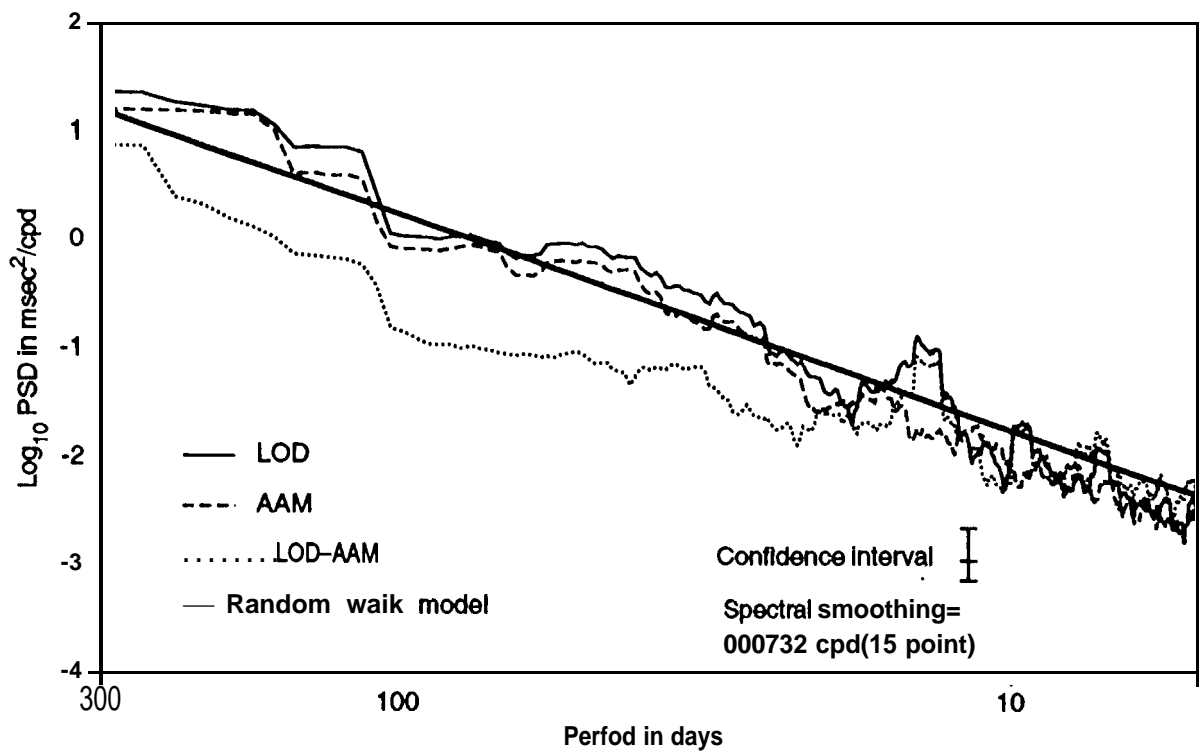
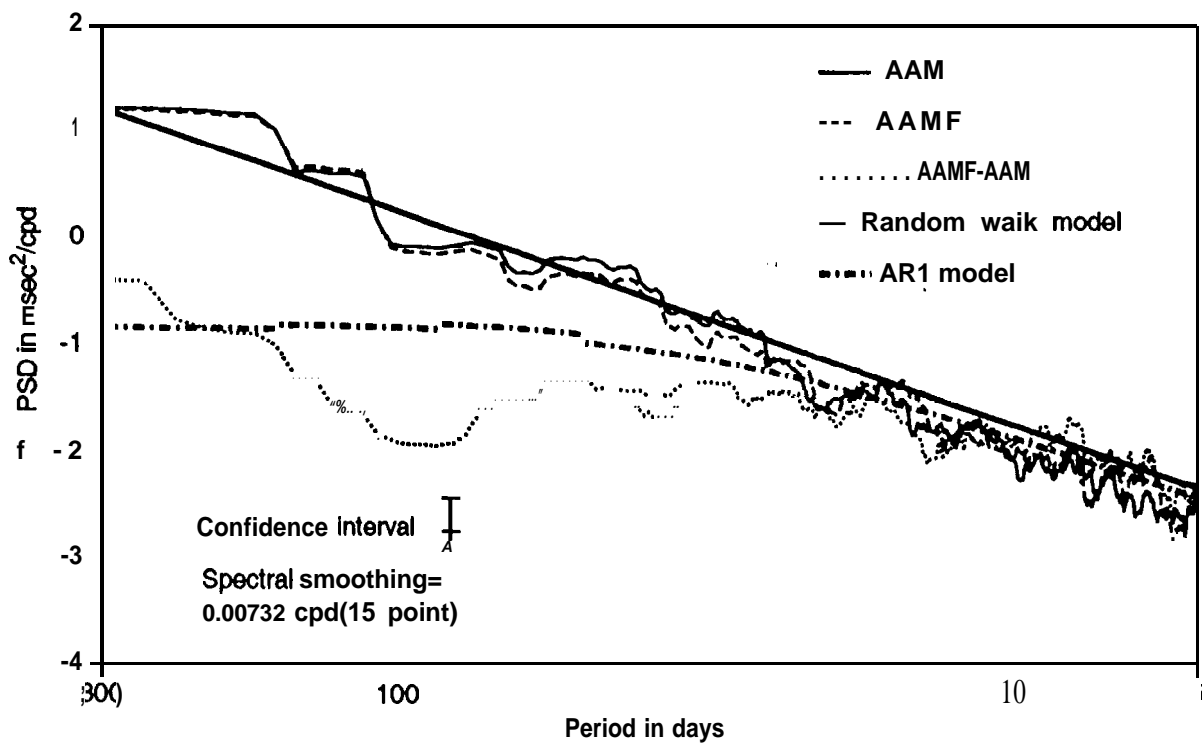


Figure 1b

PERIOD N DAYS

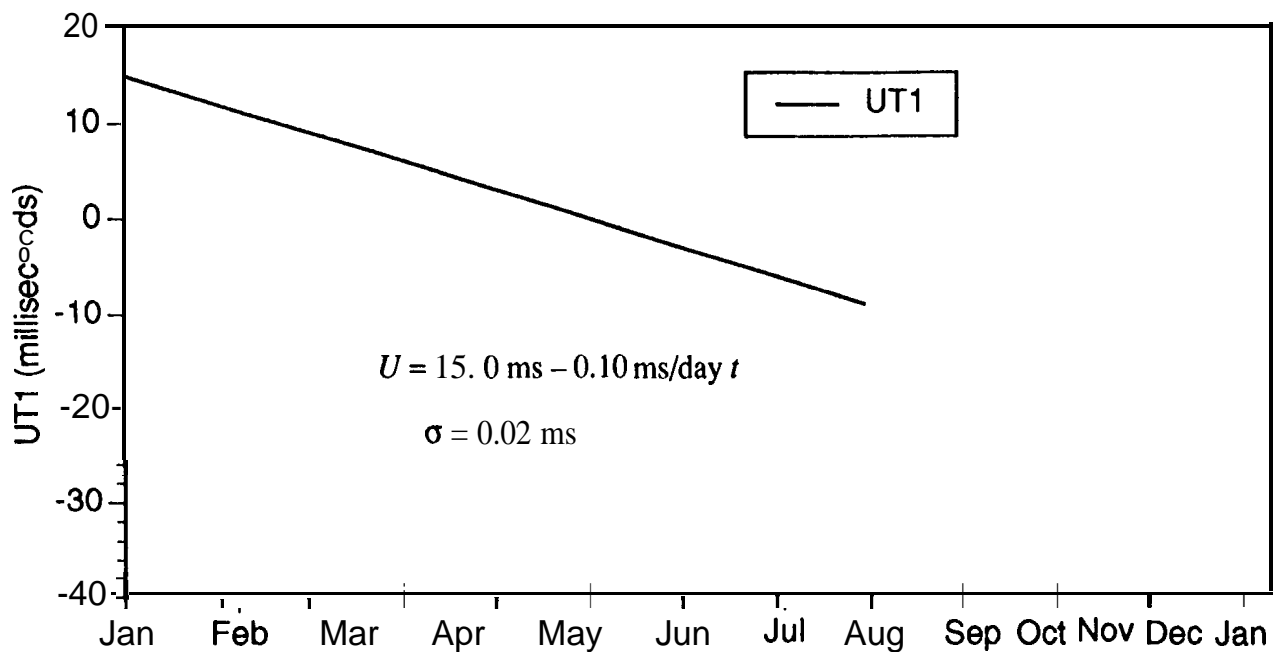


a)

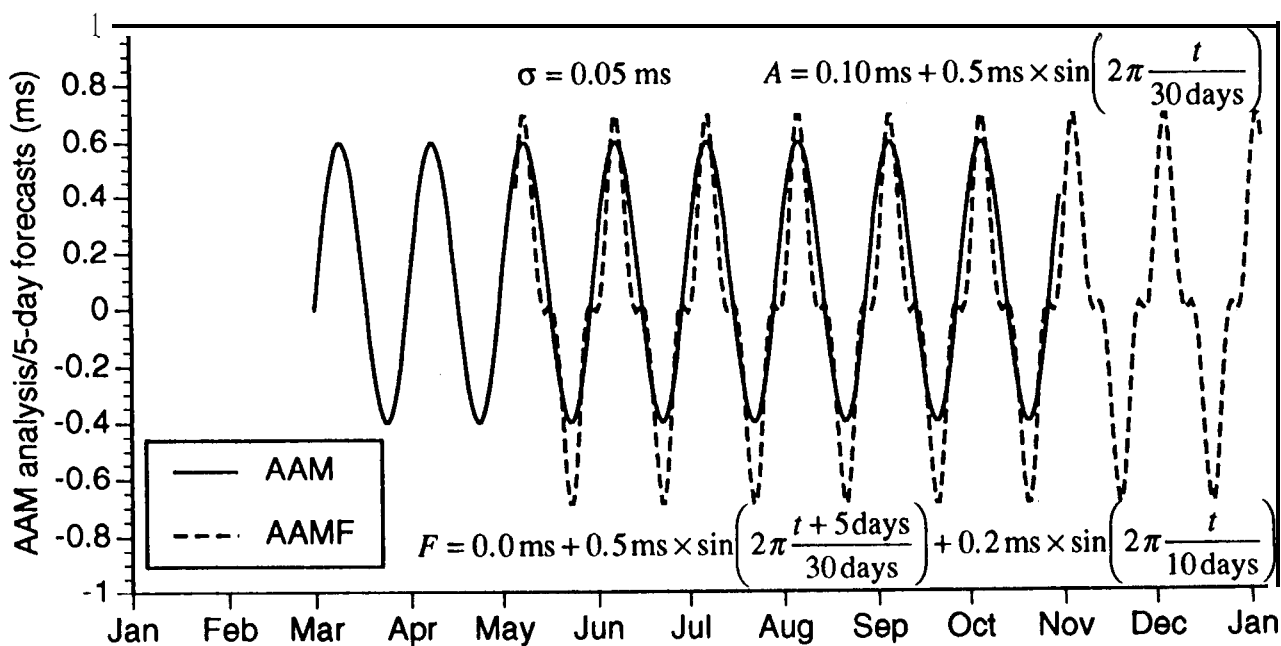


b)

FIGURE 2



a)



A)

FIGURE 3

FIGURE 4 (a,b)

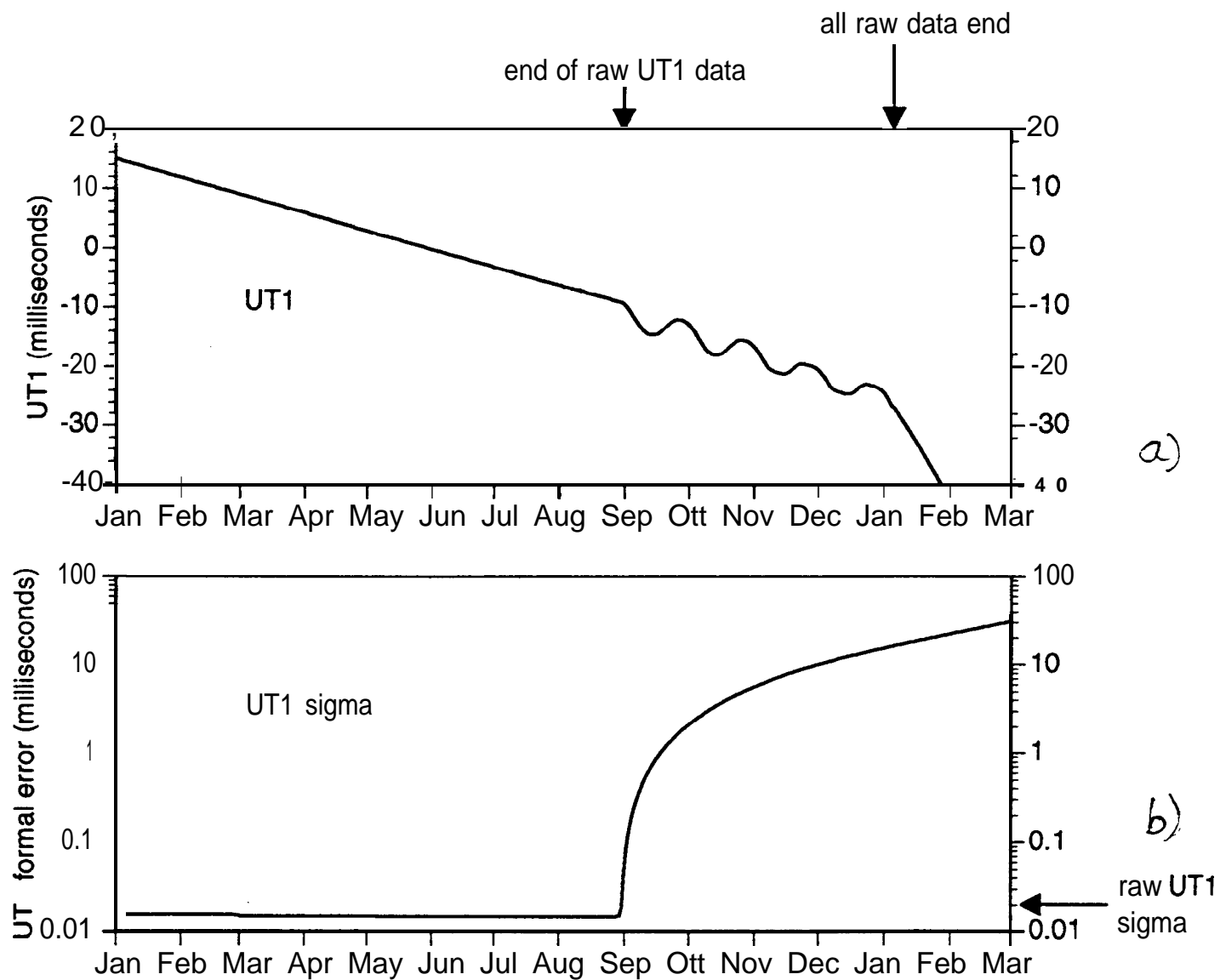
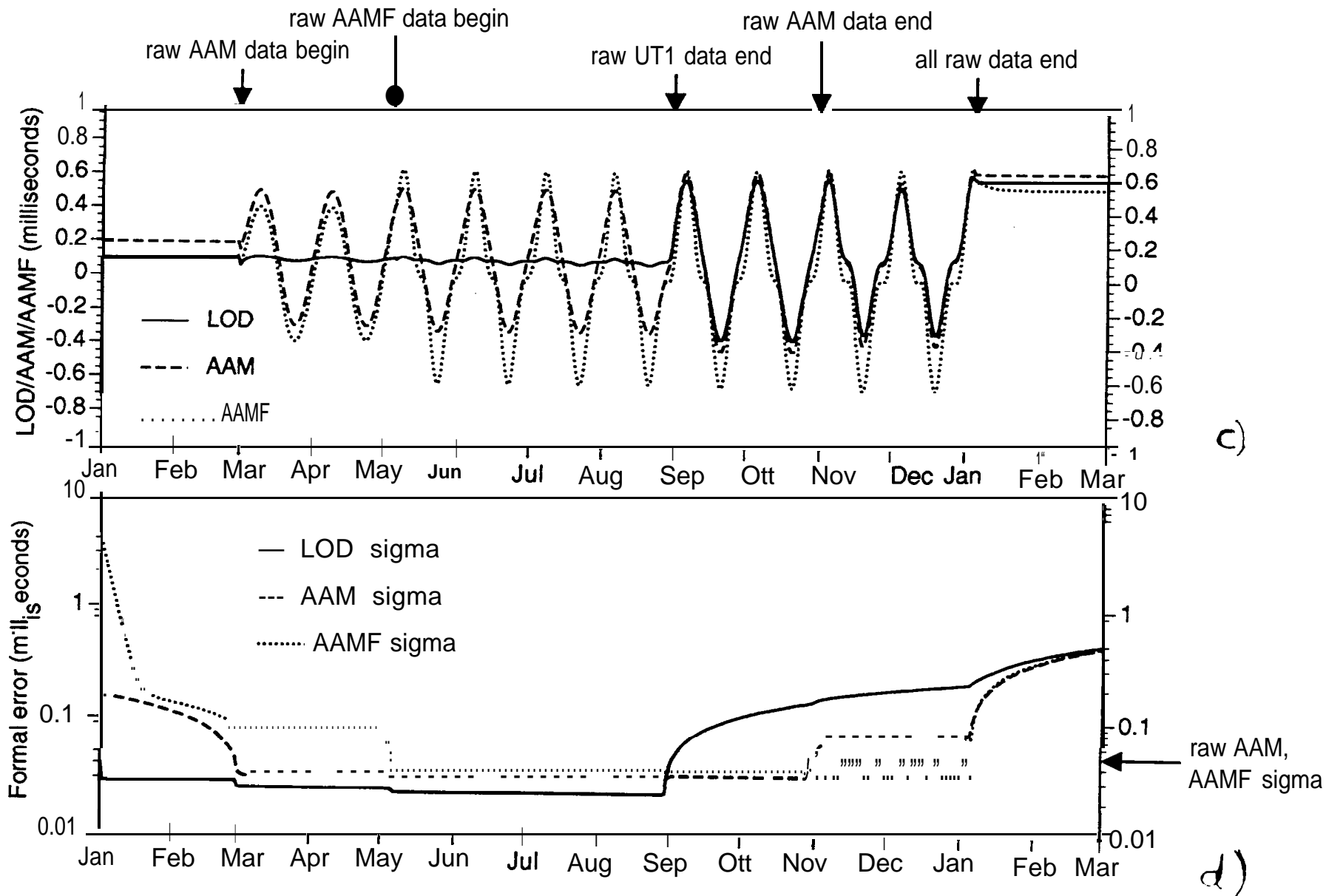


FIGURE 4 (c,d)



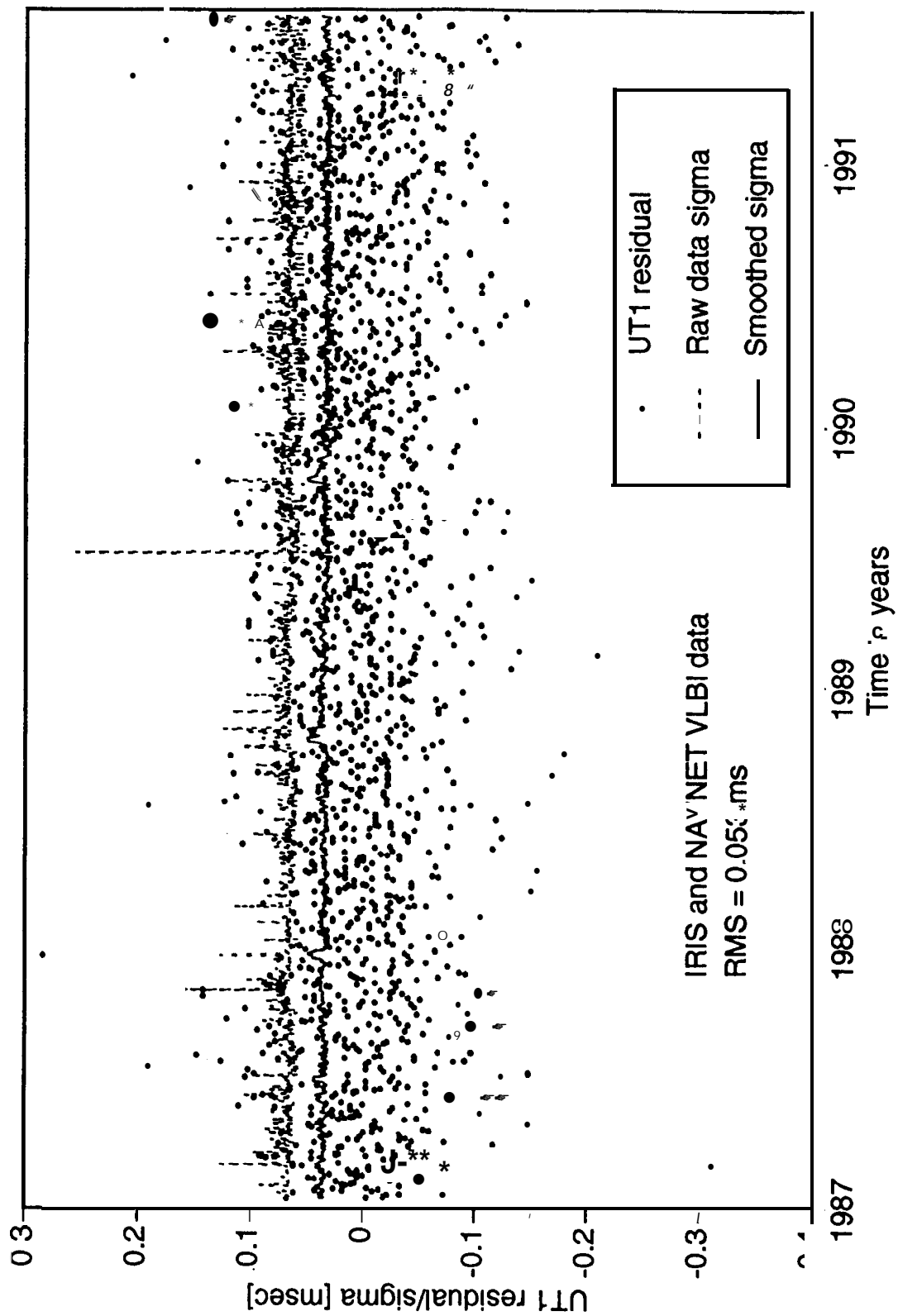


FIGURE 5

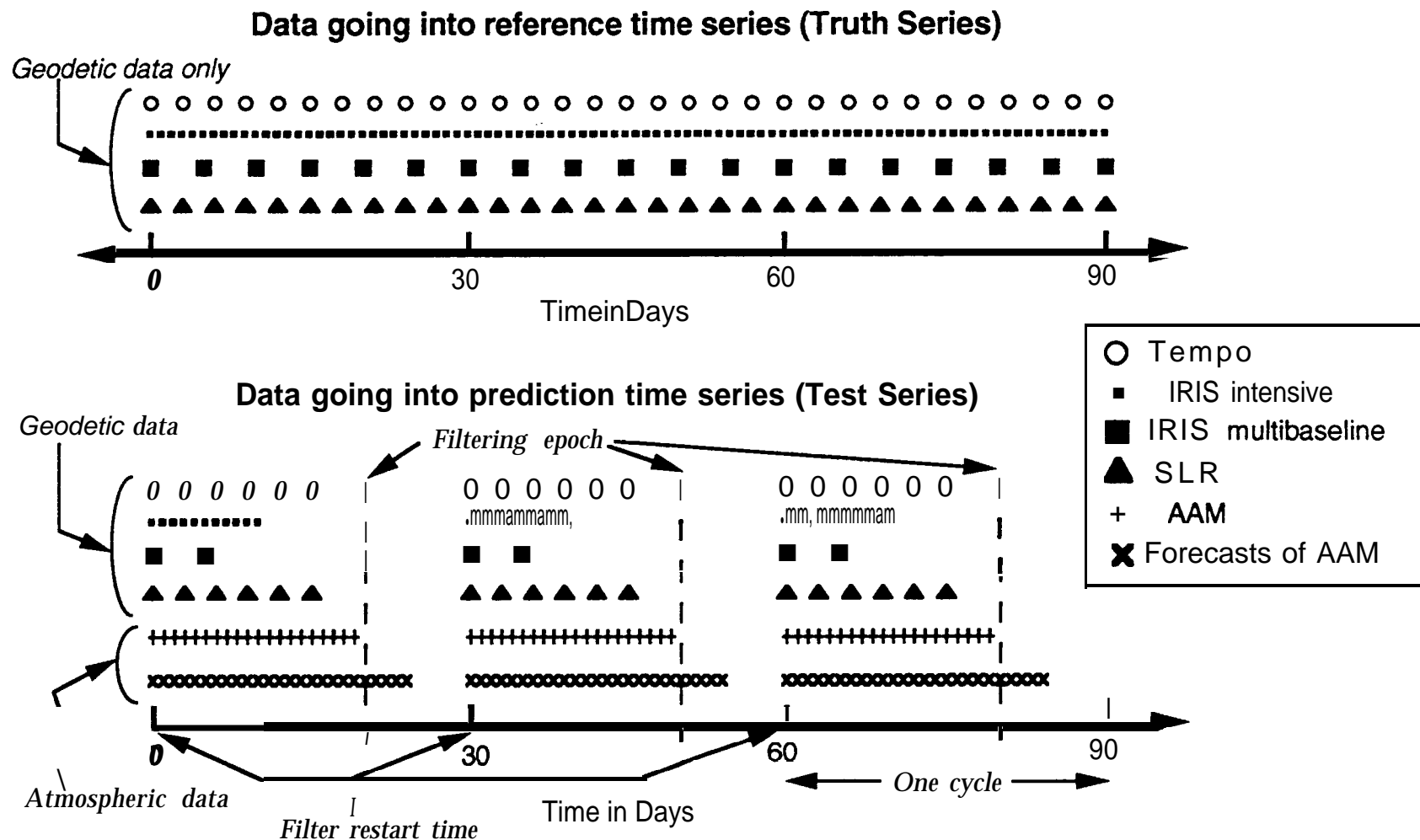


FIGURE 7

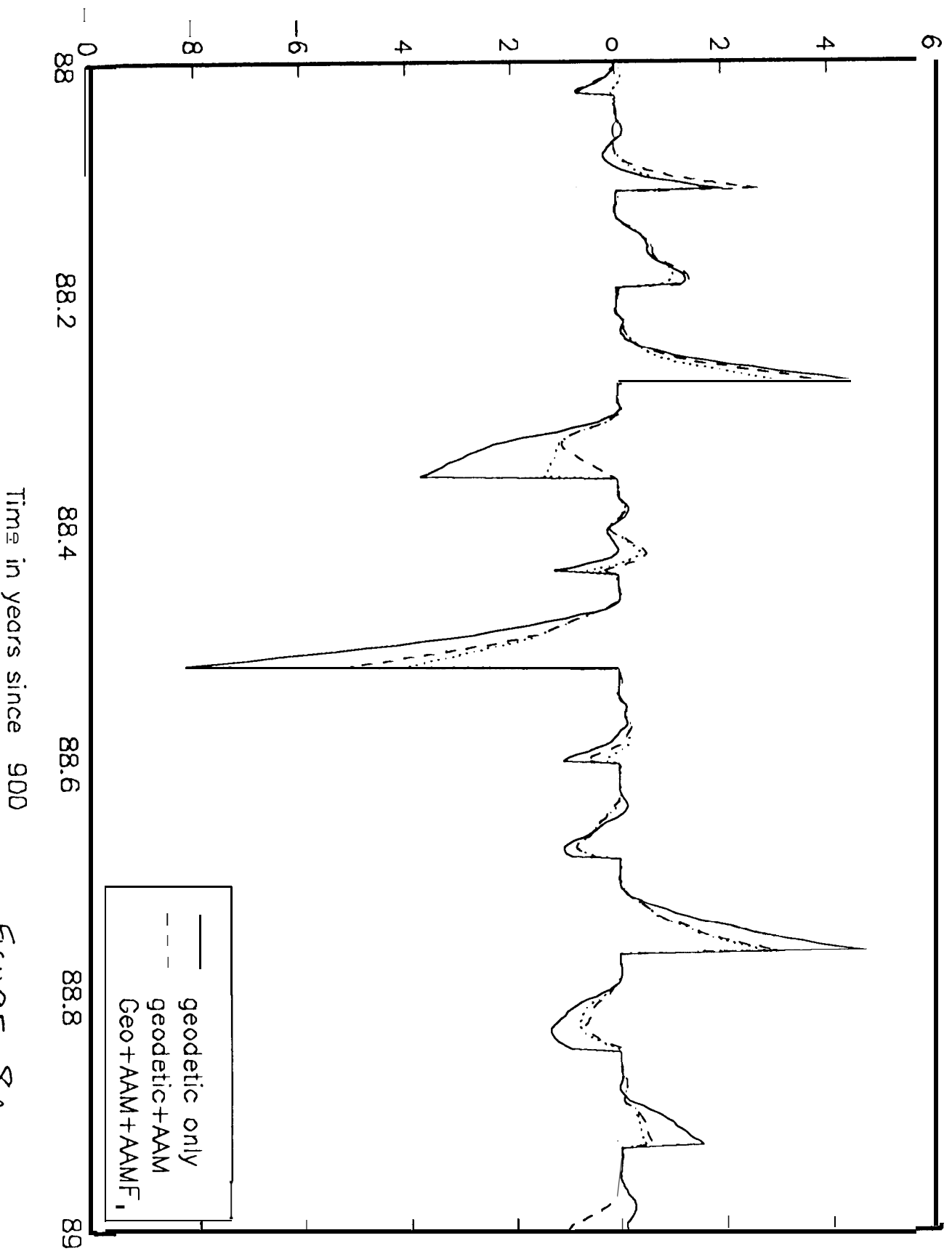


Figure 8A

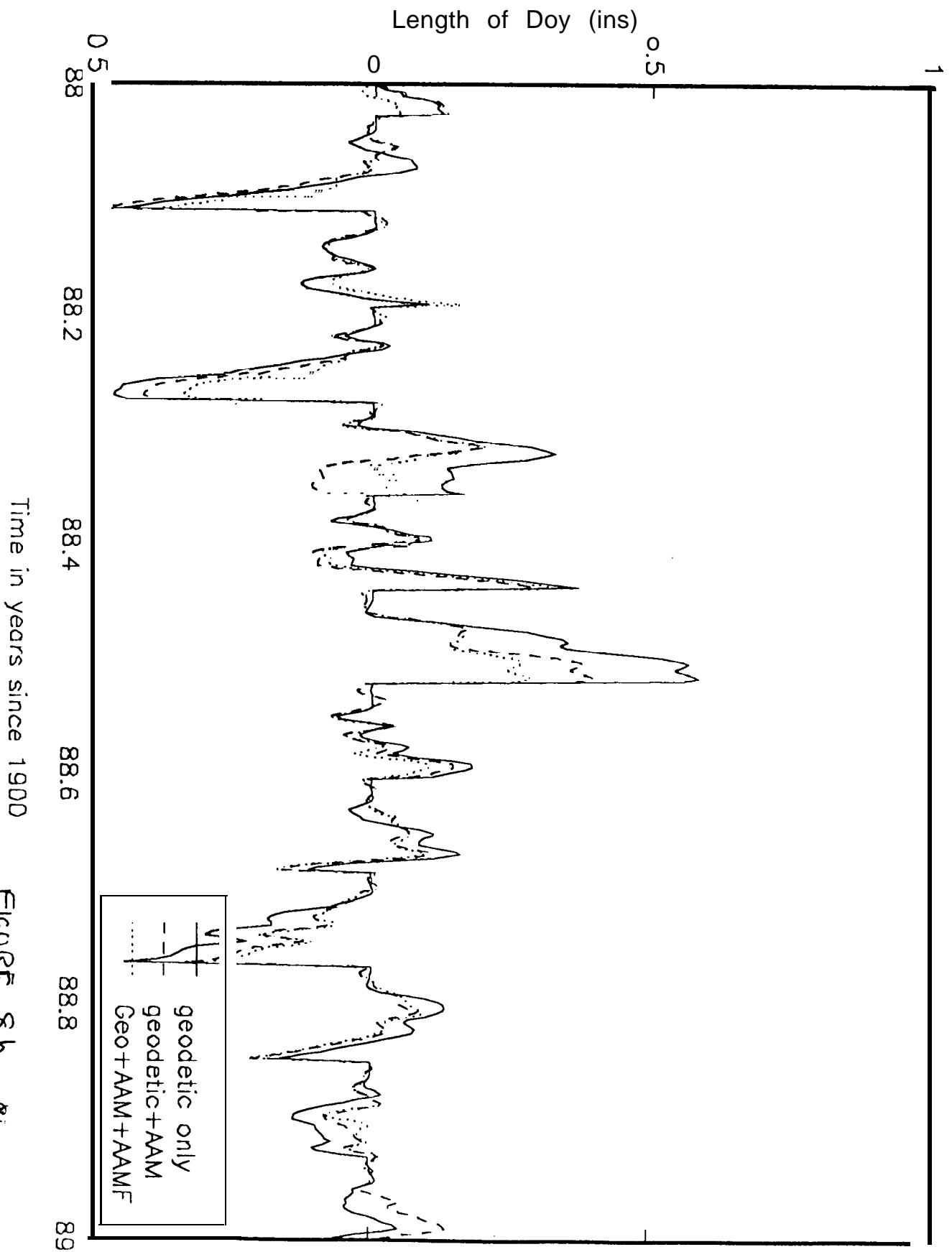


FIGURE 8b

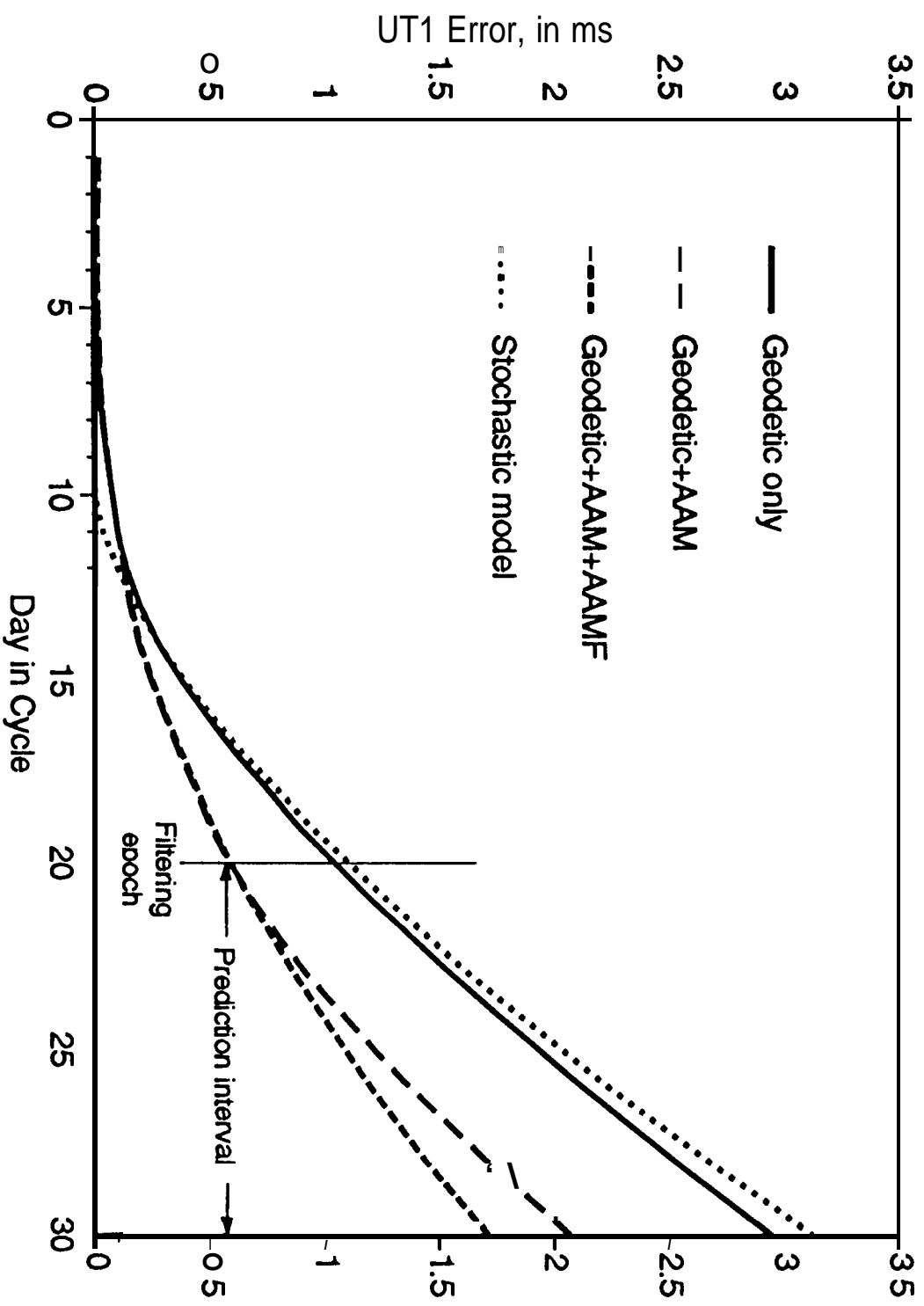


Figure 9a

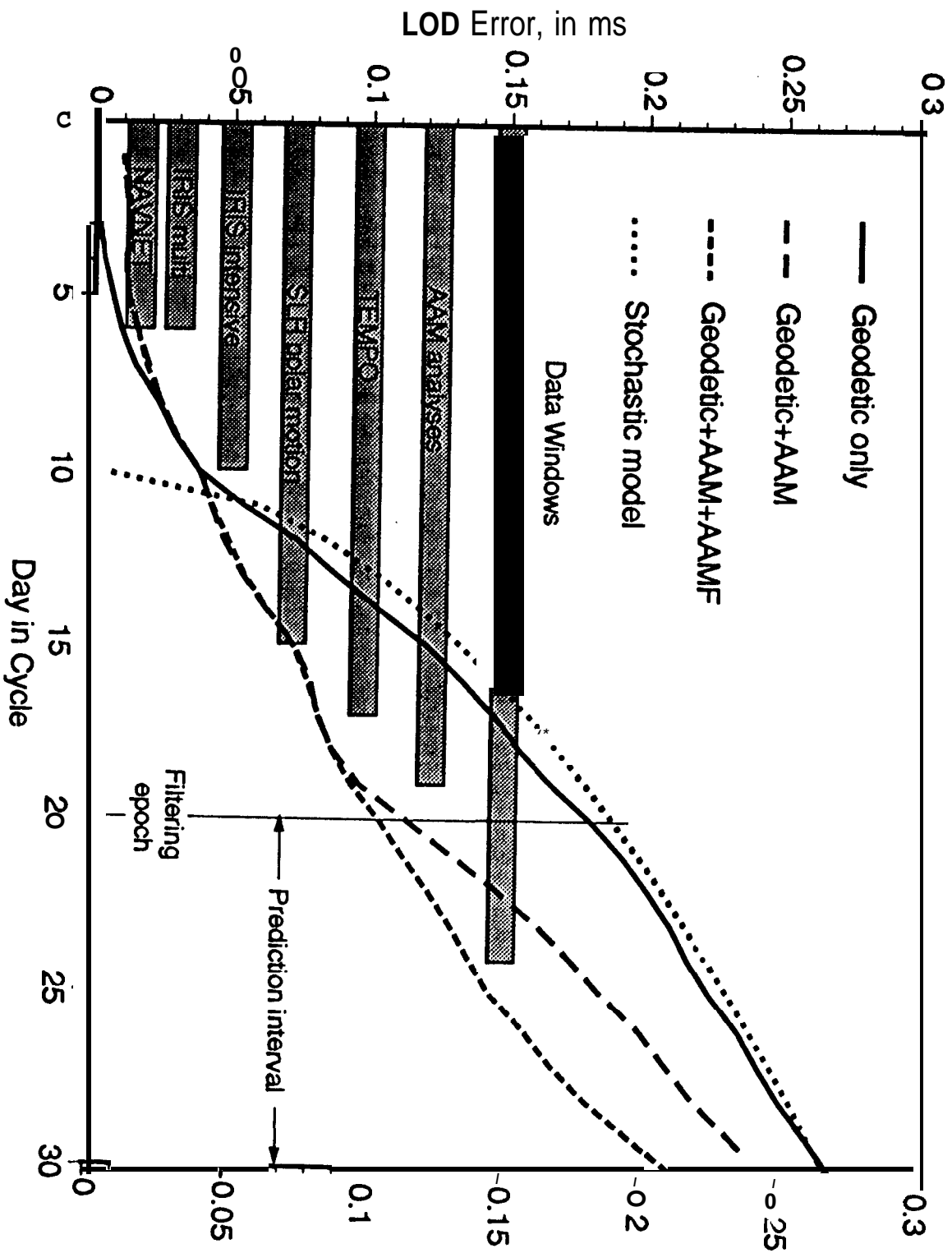


FIGURE 9b

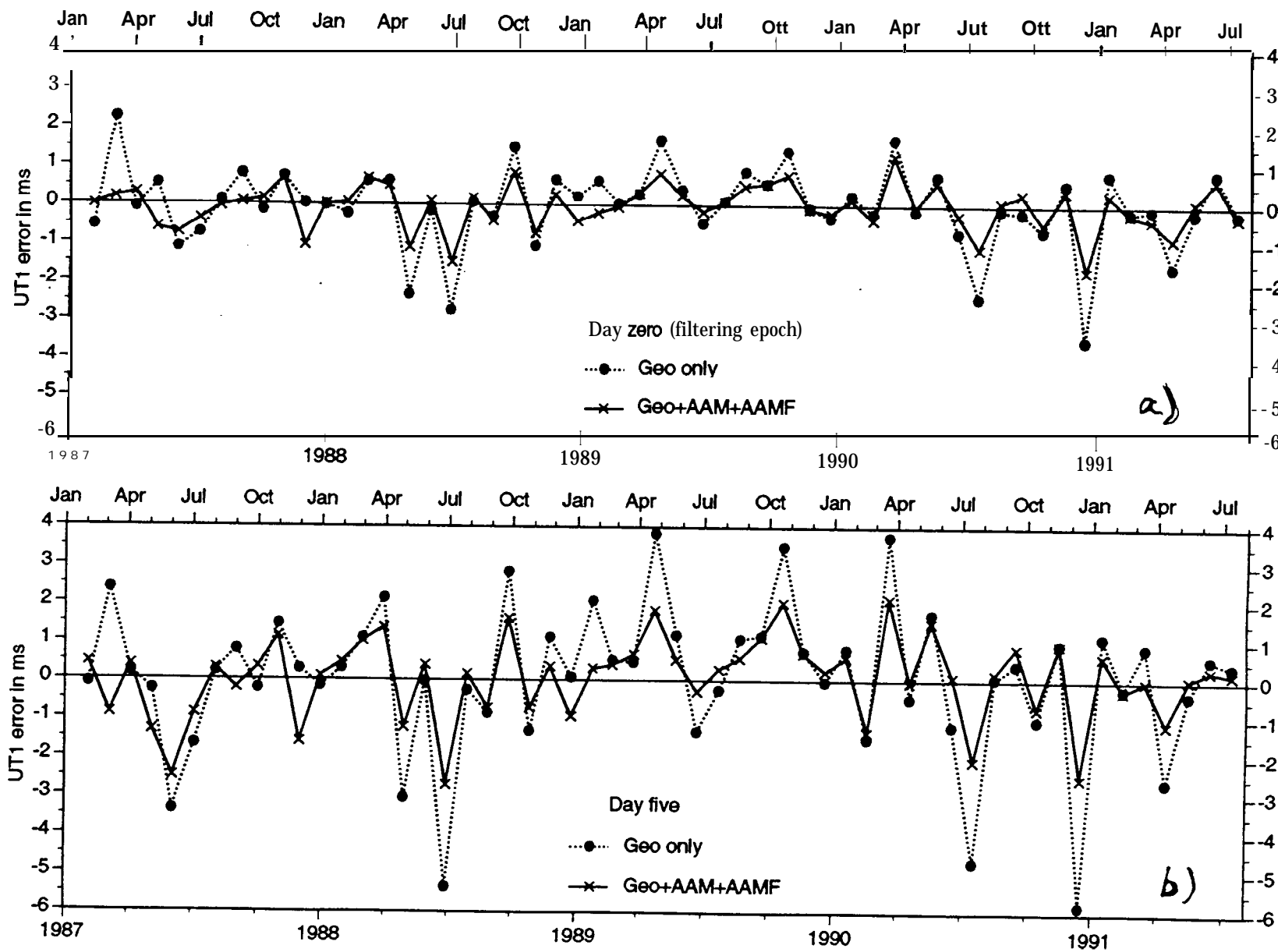


Figure 10

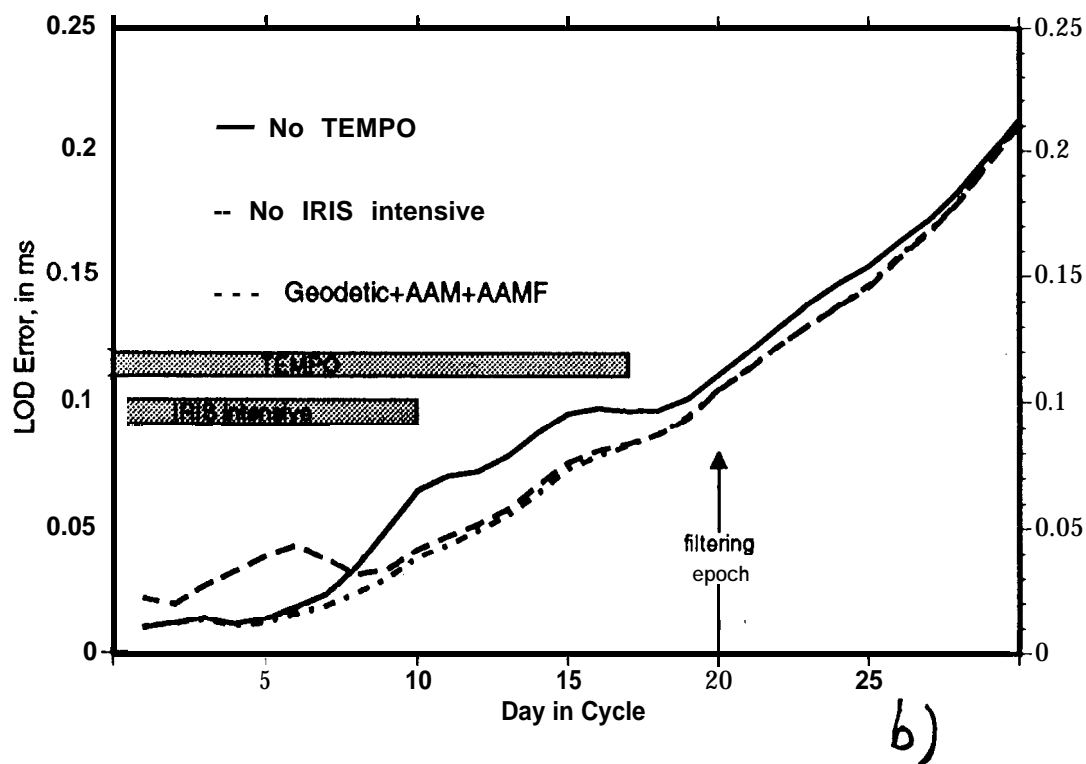
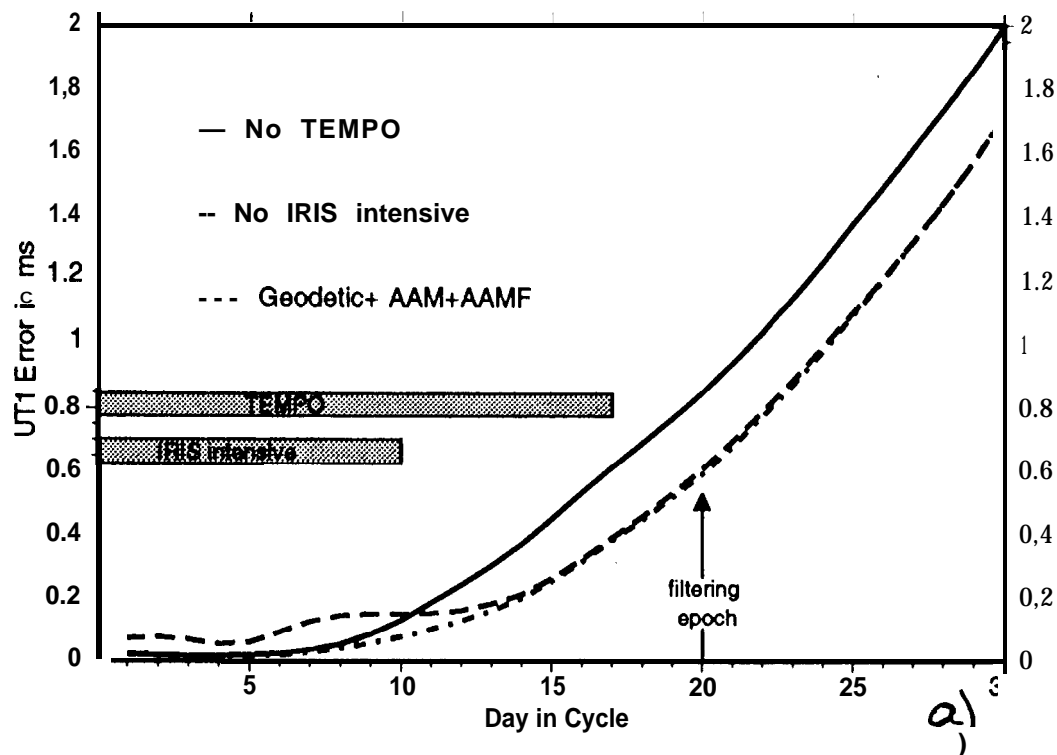


Figure 11

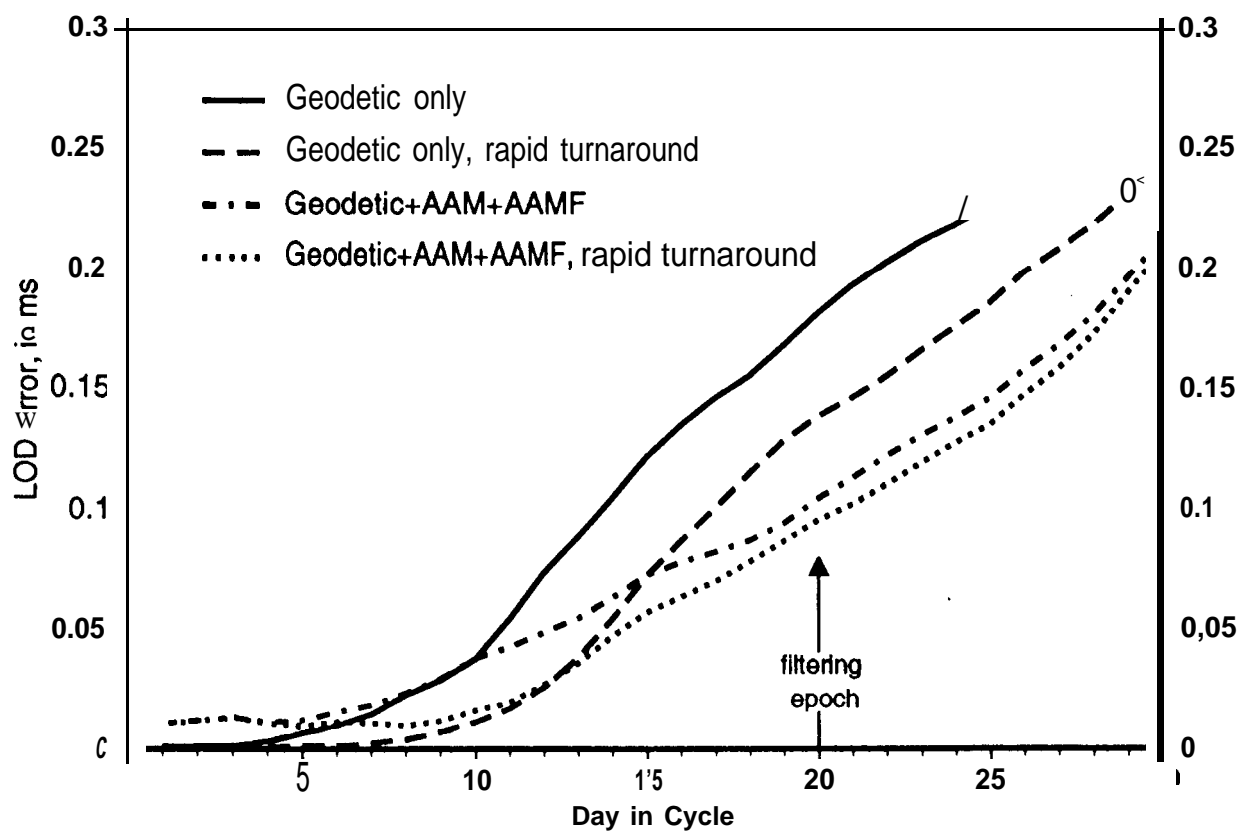
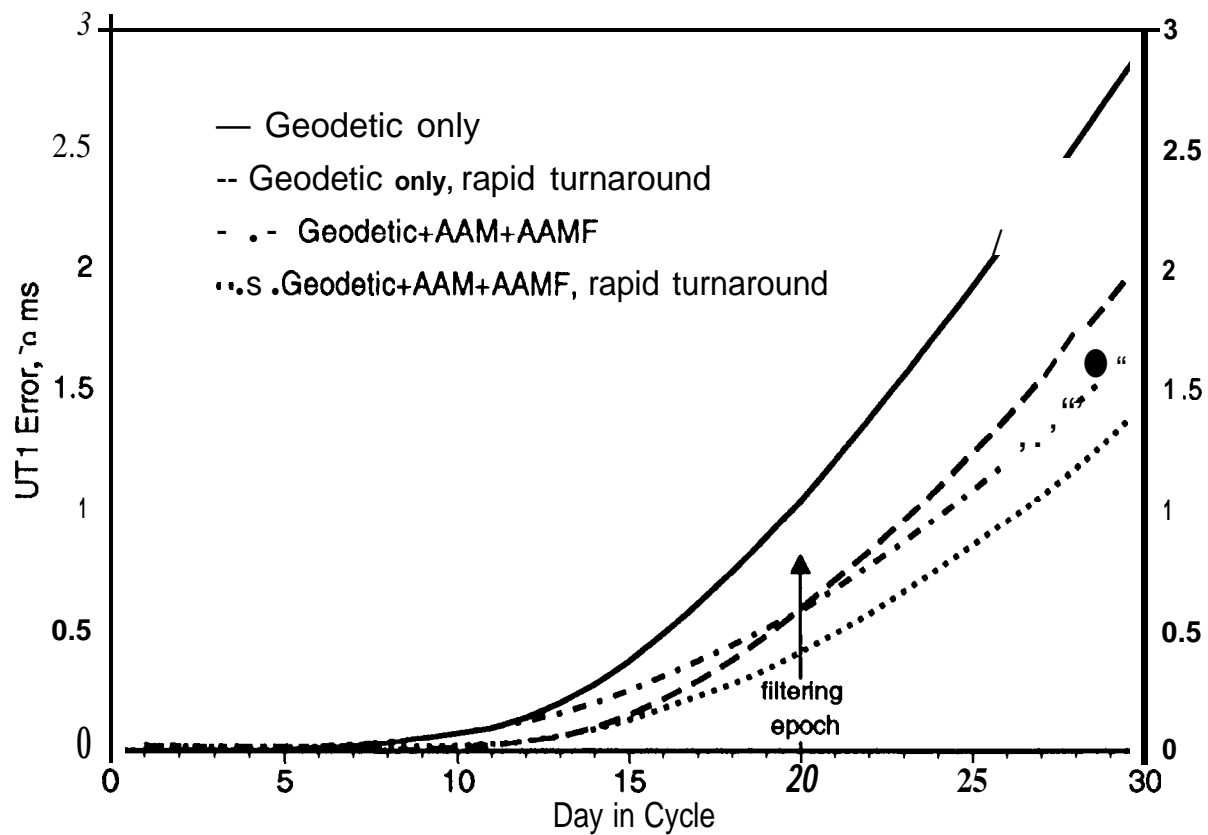


FIGURE 12

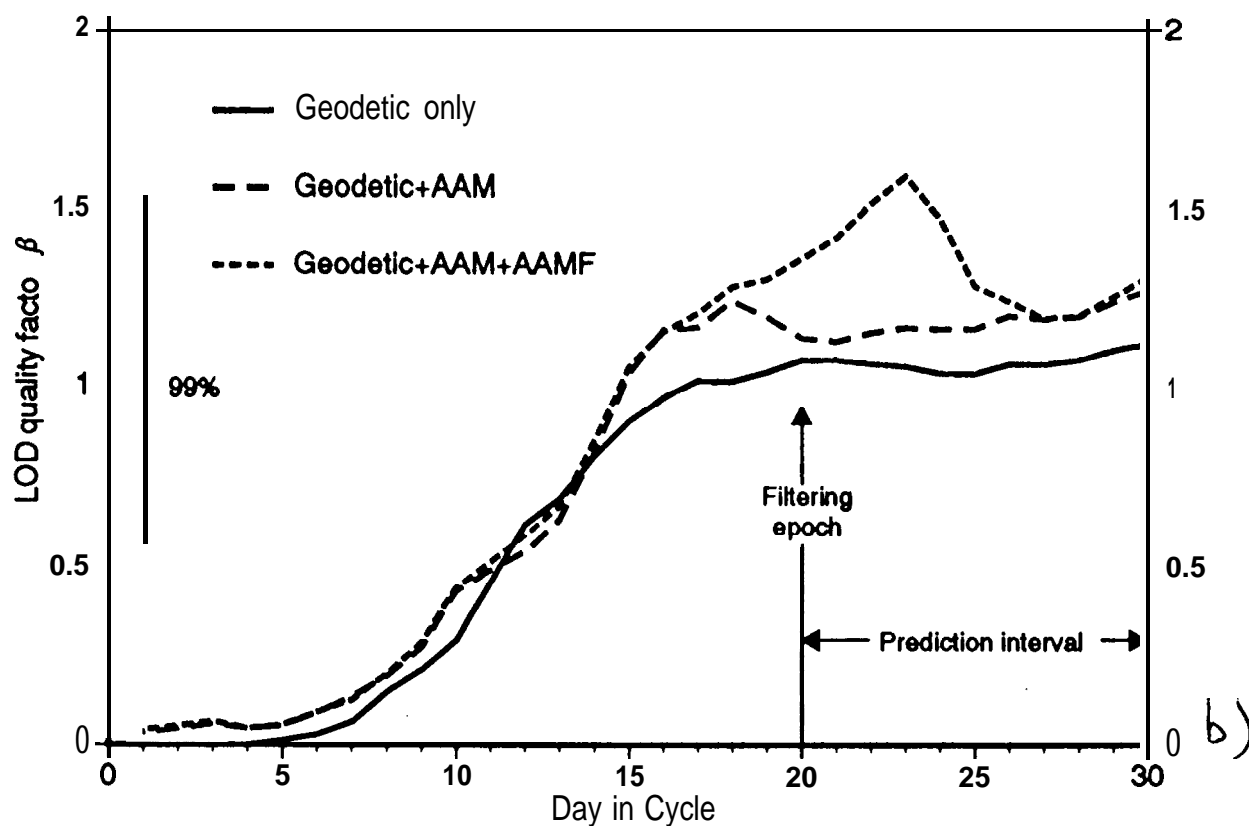
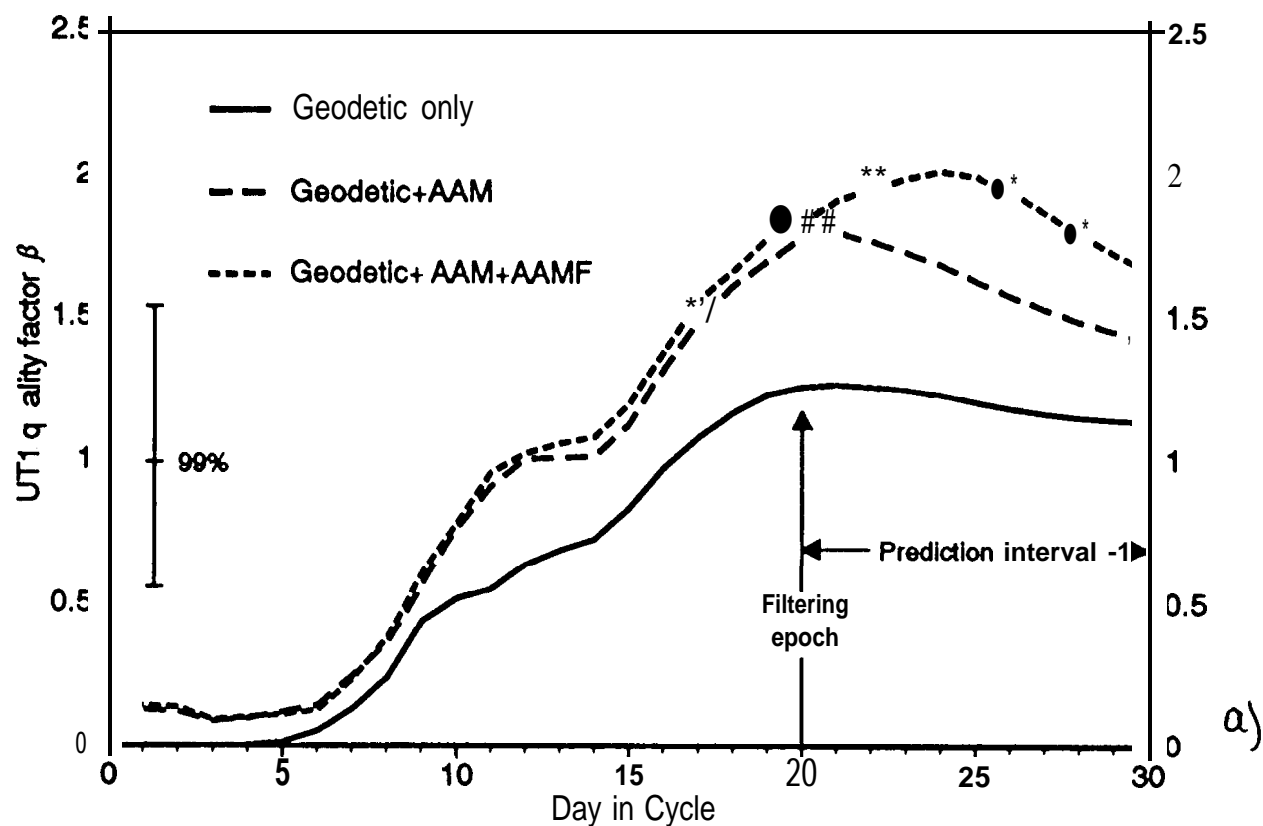


FIGURE 13

Figure 14

